J. Fluid Mech. (1988), *vol.* 191, *pp.* 79–109
Printed in Great Britain

Flow in a tube with a small side branch

By O. R. TUTTY
Department of Aeronautics and Astronautics, The University, Southampton SO9 5NH, UK

(Received 5 March 1986 and in revised form 18 August 1987)

Atherosclerotic lesions in mammalian blood vessels show a definite spatial pattern, and it has been proposed that lesions occur preferentially in regions with a low wall shear stress. Near the entrance to an intercostal artery, lesions on the wall of the aorta occur, initially at least, downstream of the entrance. We model the flow in this region by a linear shear flow along a flat wall (the wall of the main tube/aorta) past an infinitely deep circular hole perpendicular to the wall (the side-branch/intercostal artery), with fluid being sucked into the hole. By assuming Stokes flow, the three-dimensional model problem is reduced to two independent problems on a two-dimensional domain. By addition, the solutions for these problems provide the solution for any particular side-branch flow rate. We find that the wall shear stress in the main tube is elevated upstream of the side-branch entrance, and downstream as well if the side-branch flow rate is small. However, if the flow rate in the side branch is large enough, there will be regions of both elevated and reduced wall shear stress in the main tube downstream of the side-branch entrance, including a stagnation point. The wall shear is lower downsteam than upstream unless there is no net flow into the side branch.

The solutions given apply to the case with flow out of as well as into the hole. Also, the asymptotic structure for the flow in the hole when there is no net flow into the hole, and the analysis of three-dimensional flow near a sharp corner, are given.

1. Introduction

In the past 15 or so years there has been considerable interest in the role of the wall shear stress in the development of atherosclerosis in mammalian blood vessels. Fry (1973) proposed that high shear levels damage the endothelium (which forms the surface of blood vessels), and lead to increased permeability of the arterial wall, and hence to atherogenesis. Conversely, Caro, Fitz-Gerald & Schroter (1971) suggested that atheromas (growths of fatty material) are initiated in regions of low shear, because the transfer of lipids (fat) from the arterial wall is altered in such regions.

This controversy has been superseded as a result of more recent studies (see Steinberg 1983 for a review of hypotheses for artherogenesis and Schettler *et al.* (1983) or Chobanian (1983) for views on the role of fluid mechanics in atherogenesis). It is now generally accepted that the endothelial monolayer is continuous, with no evidence of cell denudation in the early stages of artherosclerosis (Schwartz, Reidy & Hansson 1983; Weinbaum *et al.* 1985). Indeed, it appears that physiological shear-stress levels are not large enough to erode endothelial cells from the wall (Nerem & Levesque 1983). It is also generally accepted that 'prelesion' or 'blue' areas of the arterial wall, which can identified by their uptake of Evans Blue dye, are preferred sites for atherosclerotic lesions. These lesions can eventually result in severe occulsion of the major blood vessels. The prelesion areas, which are characterized by an

enhanced endothelial permeability to plasma macromolecules, also have a significantly greater endothelial cell 'turnover', i.e. the cells have a shorter life (Schwartz *et al.* 1983; Weinbaum *et al.* 1985). Using a mathematical model, Weinbaum *et al.* (1985) studied the connection between cell turnover and permeability. Their results provide strong support for the theory that the increased cell turnover is responsible for the increase in permeability.

From studies of vascular casts, it appears that the shape and orientation of endothelial cells depend on the local flow conditions, with elongated cells which are aligned with the direction of the flow in regions of high shear, and rounded cells in regions of low shear (Nerem, Levesque & Cornhill 1981). This has also been found with *in vitro* studies of cultured endothelial cells (Nerem & Levesque 1983). It also appears that prelesions, and eventually atherosclerotic lesions, are more likely to occur in regions having more rounded cells (Nerem & Levesque 1983; Schwartz *et al.* 1983).

In summary, the experimental data outlined above suggest that regions of low wall shear, such as separation and reattachment points, will be susceptable to atherosclerosis. Note that while this is an attractive hypothesis supported by much experimental evidence, the evidence itself is complicated and its interpretation is by no means clear cut (see Nerem & Levesque 1983; Chobanian 1983). Indeed, one of the problems is in determining which regions have high and low wall shear stress, a question addressed below for our model problem.

Of particular interest here is the study by Cornhill & Roach (1976, hereinafter referred to as CR), who measured pre-lesions in the vicinity of intercostal arteries in cholesterol-fed rabbits. The intercostal arteries branch from the thoracic aorta, and CR found lesions on the walls of the aorta distal to the intercostal ostia (i.e. downstream of the entrance). Similar patterns have been found in humans (Sinzinger, Silberbauer & Auerswald 1980), and pigs (see Chobanian 1983).

CR interpreted their results as supporting Fry's high-shear hypothesis. However, as pointed out by Sobey (1977), CR's interpretation is based on a comparison with flow in the special case of a symmetric bifurcation, whereas a branch formed by the descending aorta and an intercostal artery is far from symmetric. In particular, the bifurcation has the form of a relatively straight main tube (the aorta) with a much smaller side branch (an intercostal artery), with only a small fraction of the flow in the main tube being diverted into a side branch. In the rabbits studied by CR, the intercostal arteries have a radius of about 0.16 mm, approximately $\frac{1}{10}$th of the radius of the aorta at the bifurcation.

The model used in this study is a straight main tube with a much smaller side branch perpendicular to it. Provided that the side-branch radius and flow rate are small enough, there will be Stokes flow near the mouth of the side branch, and the main tube wall will be a flat plate at leading order (see §2 below). Sobey (1977) considered the two-dimensional version of this problem, with a simple shear flow along a flat wall past a slot. He found that the local wall shear in the main tube depends only on the transverse velocity at the mouth of the slot, and hence concluded that models such as that of Smith (1976), with the flow at the slot entrance normal to the wall of the main tube, are unlikely to be accurate very near the slot. Sobey also found that Smith's solution, derived using boundary-layer theory, is a good approximation far from the slot.

In the present work, the three-dimensional version of Sobey's problem is considered, i.e. we assume a circular main tube with a circular side branch perpendicular to the main tube, and then study the flow near the entrance to the side

branch. The local Stokes problem, which was formulated by Pedley (1980, p. 276), is that of a linear shear flow along a flat wall past the mouth of a circular pipe set into, and normal to, the flat wall. Pedley also presented an analysis of the far field where the Stokes equations are not applicable. This analysis implies that the wake in the main tube downstream of the side branch has a complicated structure. One result of the present work is the calculation of a previously unknown parameter appearing in Pedley's asymptotic solution (see §2).

By Fourier analysis, our problem reduces to two indepedent problems on a two-dimensional domain. These problems are reformulated and some preliminary analysis is given in §2. The numerical method used is detailed in §3, and the results are presented in §4 and discussed in §5, where their physiological relevance is considered. Appendix A gives the eddy structure found in the side branch if there is no net flow down the side branch, and Appendix B examines the nature of three-dimensional flow near a sharp corner.

2. Formulation

Suppose that a circular pipe of radius a^* with velocity $O(U^*)$ has a small circular side branch, perpendicular to the main tube, of radius $b^* = \delta a^*$ with velocity $O(\delta U^*)$, where $\delta \ll 1$. Then, if

$$Re_s = \delta^2 Re \ll 1, \tag{2.1}$$

where Re_s and $Re = \rho U^* a^*/\mu$ are the side-branch and main-tube Reynolds numbers respectively, the flow near the side branch is governed at leading order by the Stokes equations, i.e.

$$\nabla \cdot \boldsymbol{u} = 0, \tag{2.2a}$$

and

$$\nabla^2 \boldsymbol{u} - \nabla p = 0. \tag{2.2b}$$

Here $\boldsymbol{x}^* = \delta a^* \boldsymbol{x}$, $\boldsymbol{u}^* = \delta U^* \boldsymbol{u}$, $p^* = (\mu U^*/a^*)p$; p^* is the pressure, and ρ and μ are the density and viscosity of the fluid respectively. The origin for $\boldsymbol{x}$ is taken as the centre of the mouth of the side branch, and, to leading order in the neighbourhood of the junction (i.e. where $\boldsymbol{x} = O(1)$), the wall of the main tube is the plane $x = 0$ (see figure 1).

To leading order the undisturbed flow in the main tube near the wall will be shear flow, and the flow down the side branch will tend to Poiseuille flow. Therefore the boundary conditions are

$$\boldsymbol{u} \to (0, -x, 0) + o(x) \quad \text{as } r^2 + x^2 \to \infty, \tag{2.3a}$$

$$\boldsymbol{u} = 0 \quad \text{on } x = 0,\ r \geqslant 1, \tag{2.3b}$$

in the main tube ($x \leqslant 0$), and

$$\boldsymbol{u} = 0 \quad \text{on } r = 1, \tag{2.3c}$$

$$\boldsymbol{u} \to (Q_b U_s(r), 0, 0) \quad \text{as } x \to \infty, \tag{2.3d}$$

in the side branch ($x > 0, r \leqslant 1$), where $y = r\cos\theta$, $z = r\sin\theta$, $U_s(r) = 4(1-r^2)$, and Q_b is the one free parameter in the problem.

Equations (2.2) and (2.3) define the Stokes problem with which this study is concerned. A formal expansion could be made in terms of δ and Re, but the order of the minor terms will depend on the magnitude of δRe – if $1 \ll \delta Re \ll \delta^{-1}$ then the next term is of $O(Re_s)$ and comes from the inertia of the fluid, while if $\delta Re \ll 1$ the next term is $O(\delta)$ from the matching to the flow in the main tube and the curvature of the wall.

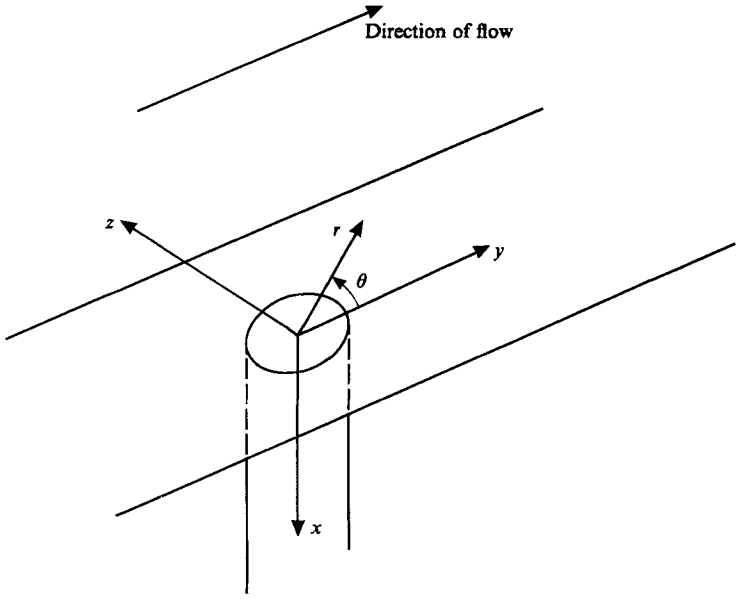

FIGURE 1. Coordinate system.

The terms $o(x)$ in (2.3a) are important, and ensure that overall continuity is satisfied, i.e. that the flow in the main tube allows for the flow down the side branch, which has mass flow rate $2\pi Q_b$. These terms are given below. Note that the ratio of the mass flow in the side branch to that in the main tube is $O(\delta^3)$.

Note also that, because of linearity, the problem can be split into two independent problems each satisfying the no-slip condition, a problem with shear flow past the side branch with no net flow into the side branch (obtained by setting $Q_b = 0$ above), and an axisymmetric problem with fluid being sucked into the side branch from the half-space. The solution for non-zero Q_b is then found by superposition. This procedure is used to simplify the calculations (see below).

2.1. *Analytical results*

Various analytical formula are available for the solution of (2.2) and (2.3), both in polar (Parmet & Saibel 1965; Lew & Fung 1969; Dagan, Weinbaum & Pfeffer 1982; Appendix A) and Cartesian coordinates (Sobey 1976). The Cartesian form is preferred here as the resulting formulae are easier to evaluate numerically. By making a triple transform (Fourier in y and z and Laplace in $-x$), the bounded part of the velocity in the main tube ($x \leqslant 0$),

$$\boldsymbol{U} = \boldsymbol{u} - (0, -x, 0), \tag{2.4}$$

and the pressure p are found to be

$$\boldsymbol{U} = -\frac{3}{2\pi}\iint_{-\infty}^{\infty} x(x, y-y', z-z')\, KR^{-5}\, \mathrm{d}y'\mathrm{d}z', \tag{2.5a}$$

$$p = -\frac{3}{\pi}\iint_{-\infty}^{\infty} [xKR^{-5} - \tfrac{1}{3}u_x(0, y', z')\, R^{-3}]\, \mathrm{d}y'\mathrm{d}z', \tag{2.5b}$$

where,

$$K = xu_x(0, y', z') + (y-y')\, u_y(0, y', z') + (z-z')\, u_z(0, y', z'), \tag{2.6a}$$

$$R^2 = x^2 + (y-y')^2 + (z-z')^2, \tag{2.6b}$$

and $\boldsymbol{u} = (u_x, u_y, u_z)$ in $\boldsymbol{x} = (x, y, z)$ (Sobey 1976; see also Pedley 1980, p. 279). For the present problem the range of integration in (2.5) is restricted to $r < 1$. Note that (2.4)–(2.6) imply that the shear on $x = 0$ is independent of the normal velocity $u_x(0, y, z)$, and that if there is no tangential velocity at the mouth of the side branch then the wall shear in the main tube is simply that from the mainstream shear flow, i.e. $(0, -1, 0)$ (Sobey 1976, 1977). In contrast, the wall pressure in the main tube comes from the normal velocity alone, and is independent of the tangential velocity.

2.2. *Formulation in cylindrical polars*

First, let us reformulate the problem in velocity–vorticity terms, since these variables are used for most of the numerical calculations: let

$$\boldsymbol{\zeta} = \nabla \times \boldsymbol{u}, \tag{2.7}$$

where $\boldsymbol{\zeta}$ is the vorticity of the fluid. Taking the curl of (2.7), and using the continuity equation (2.2*a*) gives

$$\nabla^2 \boldsymbol{u} = -\nabla \times \boldsymbol{\zeta}, \tag{2.8}$$

while eliminating the pressure from the momentum equation (2.2*b*) yields the vorticity transport equation:

$$\nabla^2 \boldsymbol{\zeta} = \boldsymbol{0}. \tag{2.9}$$

Now, take $\boldsymbol{u} = (u, v, w)$ and $\boldsymbol{\zeta} = (\xi, \eta, \zeta)$ in cylindrical polars (x, r, θ). Then, expanding in a Fourier series, the velocity and vorticity reduce to

$$(u, v, \zeta) = Q_b(u_0(x, r), v_0(x, r), \zeta_0(x, r)) + (u_1(x, r), v_1(x, r), \zeta_1(x, r)) \cos\theta, \tag{2.10a}$$

$$(w, \xi, \eta) = (w_1(x, r), \xi_1(x, r), \eta_1(x, r)) \sin\theta, \tag{2.10b}$$

all other terms being zero. Likewise, the pressure is given by

$$p(x, r, \theta) = Q_b p_0(x, r) + p_1(x, r) \cos\theta. \tag{2.10c}$$

Substitution of (2.10) in (2.7) and (2.8) along with the continuity equation (2.2*a*) produces a system of nine partial differential equations for the nine dependent variables. As mentioned above, the problem can be split into two independent problems. The axisymmetric problem (A) of flow entering the side branch from the main tube involves the variables with subscript zero only, and has as governing equations

$$(\boldsymbol{I}\nabla^2 + \boldsymbol{g})\boldsymbol{F} = \boldsymbol{G}, \tag{2.11}$$

where $\boldsymbol{I}$ is the 3×3 identity matrix, $\boldsymbol{g}$ is a 3×3 matrix with all elements zero except:

$$g_{22} = g_{33} = -\frac{1}{r^2}, \tag{2.12a}$$

the vectors $\boldsymbol{F}$ and $\boldsymbol{G}$ are

$$\boldsymbol{F} = (u_0, v_0, \zeta_0)^{\mathrm{T}}, \tag{2.12b}$$

$$\boldsymbol{G} = \left(-\frac{1}{r}\frac{\partial}{\partial r}(r\zeta_0), \frac{\partial \zeta_0}{\partial x}, 0\right)^{\mathrm{T}}, \tag{2.12c}$$

and

$$\nabla^2 = \frac{\partial^2}{\partial r^2} + \frac{1}{r}\frac{\partial}{\partial r} + \frac{\partial^2}{\partial x^2}$$

is the axisymmetric Laplacian. Also, from (2.7),

$$\zeta_0 = \frac{\partial v_0}{\partial x} - \frac{\partial u_0}{\partial r}. \tag{2.13}$$

The $o(x)$ terms in (2.3a) can be obtained from (2.4)–(2.6) and (2.10) by expanding for $R_0 = (r^2+x^2)^{\frac{1}{2}} \gg 1$. The boundary conditions for Problem A then become

$$u_0 = v_0 = 0 \quad \text{on } x = 0,\ r \geqslant 1, \quad r = 1,\ x > 0, \tag{2.14a}$$

$$v_0 = \zeta_0 = 0 \quad \text{at } r = 0, \tag{2.14b}$$

$$u_0 \to U_S(r), \quad v_0 \to 0 \quad \text{as } x \to \infty,\ r \leqslant 1, \tag{2.14c}$$

and as $R_0 \to \infty$

$$u_0 = -3\frac{x^3}{R_0^3} + 3Q_1\frac{x^2}{R_0^5}\left(1-\frac{5}{2}\frac{r^2}{R_0^2}\right) + \tfrac{15}{2}Q_2\frac{x^3}{R_0^7}\left(1-\frac{7}{2}\frac{r^2}{R_0^2}\right)+\ldots, \tag{2.14d}$$

$$v_0 = -3\frac{x^2 r}{R_0^5} - 3Q_1\frac{xr}{R_0^5}\left(1-\frac{5}{2}\frac{r^2}{R_0^2}\right) - \tfrac{15}{4}Q_2\frac{x^2 r}{R_0^7}\left(3-7\frac{x^2}{R_0^2}\right)+\ldots, \tag{2.14e}$$

where

$$Q_1 = \int_0^1 \rho^2 v_0(0,\rho)\,\mathrm{d}\rho, \quad Q_2 = \int_0^1 \rho^3 u_0(0,\rho)\,\mathrm{d}\rho. \tag{2.14f}$$

Condition (2.14b) has been obtained from the Taylor series for $r \ll 1$ and the governing equations.

The non-axisymmetric 'zero-suction' problem (C) of shear flow past the side branch involves the variables in (2.10) with subscript one only, and has as governing equations (2.11) where $\boldsymbol{I}$ is now the 6×6 identity matrix and $\boldsymbol{g}$ is a 6×6 diagonal matrix with non-zero elements

$$2g_{11} = g_{22} = g_{33} = 2g_{44} = g_{55} = g_{66} = -\frac{2}{r^2}, \tag{2.15a}$$

and the vectors

$$\boldsymbol{F} = (u_1,\ v_1,\ w_1,\ \xi_1,\ \eta_1,\ \zeta_1)^{\mathrm{T}} \tag{2.15b}$$

and

$$\boldsymbol{G} = \left(\frac{1}{r}\eta_1 - \frac{1}{r}\frac{\partial}{\partial r}(r\zeta_1),\ \frac{\partial\zeta_1}{\partial x} - \frac{1}{r}\xi_1 + \frac{2}{r^2}w_1,\ \frac{\partial\xi_1}{\partial r} - \frac{\partial\eta_1}{\partial x} + \frac{2}{r^2}v_1,\ 0, -\frac{2}{r^2}\zeta_1,\ -\frac{2}{r^2}\eta_1\right)^{\mathrm{T}}. \tag{2.15c}$$

The vorticity is

$$(\xi_1, \eta_1, \zeta_1) = \left(\frac{1}{r}\frac{\partial}{\partial r}(rw_1) + \frac{v_1}{r},\ -\frac{u_1}{r} - \frac{\partial w_1}{\partial x},\ \frac{\partial v_1}{\partial x} - \frac{\partial u_1}{\partial r}\right), \tag{2.16}$$

and the boundary conditions for Problem C are

$$u_1 = v_1 = w_1 = 0 \quad \text{on } x = 0,\ r \geqslant 1, \quad r = 1, x < 0, \tag{2.17a}$$

$$u_1 = \xi_1 = 0,\ v_1 = -w_1 = -w_1,\ \eta_1 = \zeta_1 \quad \text{at } r = 0, \tag{2.17b}$$

$$u_1, v_1, w_1 \to 0 \quad \text{as } x \to \infty, r \leqslant 1, \tag{2.17c}$$

and as $R_0 \to \infty$

$$u_1 = -3\hat{Q}_1\frac{x^2 r}{R_0^5} - \tfrac{15}{2}\hat{Q}_2\frac{xr}{R_0^7} + \frac{15x^2 r}{R_0^7}(\hat{Q}_3 + \tfrac{1}{2}\hat{Q}_4)\left(1-\frac{7}{4}\frac{r^2}{R_0^2}\right)+\ldots, \tag{2.17d}$$

$$v_1 = -x - 3\hat{Q}_1\frac{xr^2}{R_0^5} + \tfrac{3}{2}\hat{Q}_2\frac{x^2}{R_0^5}\left(1-5\frac{r^2}{R_0^2}\right) - \tfrac{3}{2}(\hat{Q}_3+\hat{Q}_4)\frac{x}{R_0^5} + \tfrac{15}{2}(\hat{Q}_3+\tfrac{1}{2}\hat{Q}_4)\frac{xr^2}{R_0^7}\left(3-\frac{7}{4}\frac{r^2}{R_0^2}\right)+\ldots, \tag{2.17e}$$

$$w_1 = -x - \tfrac{3}{2}\hat{Q}_2\frac{x^2}{R_0^5} + \tfrac{3}{2}(\hat{Q}_3+\hat{Q}_4)\frac{x}{R_0^5} - \tfrac{15}{4}\hat{Q}_4\frac{xr^2}{R_0^7}+\ldots, \tag{2.17f}$$

Problem A		Problem C	
Q_1	−0.11	$\hat{Q}_1$	0.052
Q_2	0.37	$\hat{Q}_2$	−0.011
		$\hat{Q}_3$	0.020
		$\hat{Q}_4$	−0.0007

TABLE 1. Coefficients for the far-field expansion in the main tube, as defined in (2.14*f*) and (2.17*g*)

$$\text{where} \quad \hat{Q}_1 = \frac{1}{2}\int_0^1 \rho[v_1(0,\rho) - w_1(0,\rho)]\,\mathrm{d}\rho, \quad \hat{Q}_2 = \int_0^1 \rho^2 u_1(0,\rho)\,\mathrm{d}\rho,$$
$$\hat{Q}_3 = \frac{1}{2}\int_0^1 \rho^3[v_1(0,\rho) - w_1(0,\rho)]\,\mathrm{d}\rho, \quad \hat{Q}_4 = \frac{1}{2}\int_0^1 \rho^3[v_1(0,\rho) + w_1(0,\rho)]\,\mathrm{d}\rho. \tag{2.17g}$$

Note that each of the coefficients in (2.14*f* and 2.17*g*) gives a 'flow' which satisfies the continuity equation (2.2*a*), and that the flow given by the first term in each of (2.14*d*, *e*) satisfies overall continuity for the axisymmetric problem A, and is, in fact, the solution for a Stokes flow in a half-space with a point sink at the origin. Also, it is apparent from the expansions above that the behaviour of the flow in the far field in the main tube varies with x and r. For example, for $-x \gg 1$, Problem A is dominated by the first term in (2.14*d*, *e*), while close to the wall ($-x \ll 1$), the term with Q_1 is dominant (in particular, in the expansion for the shear stress on the wall). The coefficients in (2.14*f* and 2.17*g*) must be calculated interactively. Table 1 gives the values obtained numerically. We note that $2\pi\hat{Q}_1$ is the parameter K_W appearing in Pedley's (1980, p. 281) far-field asymptotic analysis.

The Stokes problem (2.2) and (2.3) has now been de-coupled into two independent Stokes problems on a two-dimensional L-shaped domain (see figure 2), and is in a form suitable for numerical computation. Neither of the problems explicitly ensures that the continuity equation (2.2*a*) and the vorticity definition (2.7) are satisfied. In general it follows that if the vorticity definition is satisfied on the boundaries, (2.2*a*) and (2.7) will be satisfied everywhere (this provides the method of calculating the boundary vorticity – see § 3). However, the sharp corner at $(x, r) = (0, 1)$ creates difficulties, a point discussed briefly in §3 below.

For later reference, with (2.10) the continuity equation reduces to

$$\frac{\partial u_0}{\partial x} + \frac{1}{r}\frac{\partial}{\partial r}(rv_0) = 0, \tag{2.18a}$$

and

$$\frac{\partial u_1}{\partial x} + \frac{1}{r}\frac{\partial}{\partial r}(rv_1) + \frac{1}{r}w_1 = 0. \tag{2.18b}$$

Also, the components of the main-tube wall shear stress are defined as $\tau_y = \partial u_y/\partial x$ and $\tau_z = \partial u_z/\partial x$ on $x = 0$, where $r > 1$, with similar definitions for τ_r and τ_θ. $\tau = (\tau_x^2 + \tau_y^2)^{\frac{1}{2}} = (\tau_r^2 + \tau_\theta^2)^{\frac{1}{2}}$ gives the magnitude of the wall shear stress. Note that with this definition the basic shear in the main tube is negative.

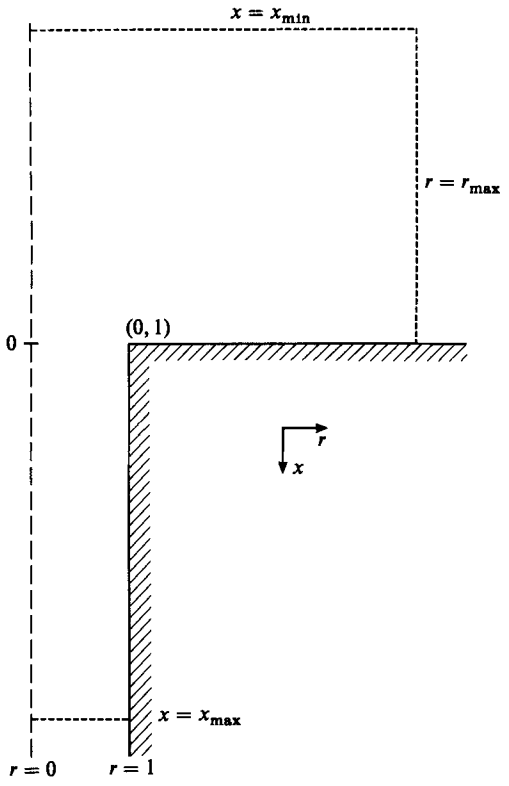

FIGURE 2. Computational domain.

3. Numerical

Equations (2.7)–(2.9) are the Stokes version of the velocity-vorticity formulation used by Dennis, Ingham & Cook (1979) to solve the steady three-dimensional driven-cavity problem in Cartesian coordinates. Their finite-difference scheme, which is second-order accurate, has diagonally dominant matrices and is stable for Reynolds numbers greater than 100. Likewise, the scheme presented below for (2.11)–(2.13) is second-order accurate and the associated matrices are diagonally dominant. Note, that, here and below, second-order accurate implies an $O(h^2)$ truncation error in the finite-difference analogue of the relevant equation.

3.1. *The basic method*

A rectangular grid $(x_i, r_j) = h(i,j)$ was used, with $i = L, L+1, \ldots, -1, 0$ and $j = 0, 1, \ldots, M$ in the main tube, and $i = 0, 1, \ldots, N$ and $j = 0, 1, \ldots, M_0$ in the side branch, where $L < 0$, M, M_0 and $N > 0$, and $h = 1/M_0$. Unless specifically mentioned, all results presented below have $N = M = -L = 4M_0$. This was found to give boundaries sufficiently distant from the side-tube entrance to allow the use of asymptotic expansions (2.14*d–f* and 2.17*d–g*) in the main tube, and to make the flow near the entrance essentially independent of the exact form of the conditions used at the bottom of the side branch (see below).

For most (i,j) in the fluid, standard central differences were used for the governing equations (2.11) with (2.12) or (2.15). An obvious exception is at $r = 0$, where these equations do not apply. Here application of L'Hôpital's rule produces the correct

limiting form for quantities not determined by (2.14*b*) and (2.17*b*), e.g. the equation for u_0 becomes

$$\frac{\partial^2 u_0}{\partial x^2} + 2\frac{\partial^2 u_0}{\partial r^2} = -2\frac{\partial \zeta_0}{\partial r},$$

which with

$$\frac{\partial u_0}{\partial r} = \frac{\partial^2 \zeta_0}{\partial r^2} = 0 \quad \text{at } r = 0,$$

gives a finite-difference equation. Another exception is at the points immediately adjacent to the corner. The singularity in the Stokes expansion (Moffatt 1964; Moffatt & Duffy 1980; see also Appendix B below) implies an infinite vorticity at the corner, which prevents the use of the standard finite-difference formulae at the points $(x, r) = (0, 1-h)$ and $(-h, 1)$. For a Navier–Stokes flow in a branching channel, Bramley & Dennis (1984) compared two basic methods for dealing with this problem – arranging the finite-difference representation so that the corner vorticity was never used, and using the Stokes expansion directly. There was good agreement between the two methods, and they concluded that either was satisfactory. The former procedure has the advantages that it does not imply a particular form for the vorticity, and that it extends simply to three-dimensional problems. It was used here, with the finite-difference molecule rotated to avoid the corner point when necessary, e.g. instead of using the values at $(i \pm 1, j)$, $(i, j \pm 1)$ and (i, j) for vorticity at $(i, j) = (0, M_0 - 1)$, the values at $(i \pm 1, j \pm 1)$ and (i, j) were used.

Apart from the matching conditions in the side branch, which are discussed below, application of the boundary conditions for the velocity components is straightforward. Simpsons rule was used to calculate the coefficients (2.14*f*) and (2.17*g*) for the far-field expansions in the main tube.

The wall vorticity was calculated from finite-difference analogues of the definitions (2.13) and (2.16) in the manner of Dennis *et al.* (1979). These formulae are in a sense the velocity–vorticity form of the stream function–vorticity formula of Woods (1954), in that they are $O(h^2)$ accurate and compact, using the velocity and vorticity at the wall and at a distance h from it. For example,

$$(\zeta_0)_{i, M_0} = -(\zeta_0)_{i, M_0 - 1} + \frac{2}{h}(u_0)_{i, M_0 - 1} \quad \text{for } i = 1, 2, \ldots, N \tag{3.1}$$

is obtained from (2.13) and the continuity equation (2.18*a*).

In the main tube, the far-field vorticity can be obtained from the asymptotic expansions for the velocity (2.14*d–f*) and (2.17*d–g*) and the definitions (2.13) and (2.16). Alternatively, formulae similar to, but more complicated than (3.1) could be used. Test runs showed that the latter method slows down the convergence rate, and does not signficantly affect the results. Hence the more direct method was used.

3.2. *Continuity*

Unfortunately, there is a serious flaw in the above finite-difference scheme, in that continuity is not satisfied locally. If the axisymmetric problem (2.11)–(2.14) is solved with, say, $h = \frac{1}{16} (= 1/M_0)$ and $N = M = -L = 4M_0$, this has the result that the mass flow at the mouth of the side branch is approximately one-quarter of that expected, i.e. the numerical solution gives

$$\int_0^1 r u_0(0, r)\, \mathrm{d}r \approx 0.23$$

instead of unity. Refining the grid while keeping the calculation domain constant does not improve matters significantly. This problem arises naturally from the corner singularity. Details will be given in a later publication.

To enforce continuity and the vorticity definition (2.13a), the governing equation for u_0 was replaced on the entrance to the side branch ($x = 0, r \leqslant 1$), by the finite-difference version of

$$\frac{\mathrm{d}^2 Q_0}{\mathrm{d}r^2} - \frac{1}{r}\frac{\mathrm{d}Q_0}{\mathrm{d}r} = r\left(\frac{\partial v_0}{\partial x} - \zeta_0\right), \tag{3.2a}$$

with

$$Q_0(0) = 0, \quad Q_0(1) = 1, \tag{3.2b}$$

and u_0 calculated from

$$U_0(0, r) = \frac{1}{r}\frac{\mathrm{d}Q_0}{\mathrm{d}r}. \tag{3.2c}$$

This was found to produce satisfactory results (see below). Note that $Q_0(r)$ is simply the standard stream function evaluated at $x = 0$, and (3.2a) is, in effect, the Poisson equation which can be used to define the vorticity in two-dimensional flow. A similar technique was used to calculate u_1 on $x = 0$; i.e. (3.2a, c) with u_1, v_1 and ζ_1, and (3.2b) replaced by $Q_0(1) = 0$ and $\mathrm{d}Q_0/\mathrm{d}r = \mathrm{d}^2 Q_0/\mathrm{d}r^2 = 0$ at $r = 0$ (from $u_1(x, 0) = 0$).

3.3. *The side branch*

In §2 above, the boundary condition down the side branch is given simply as a matching condition at infinity (equations (2.3d), (2.14c) and (2.17c)). We now consider this condition in detail.

For the axisymmetric problem A, the values at $x_{\max} = 4$ were set from Poiseuille flow. Theoretical justification for this is provided by the work of Lew & Fung (1969), who found that the deviation from Poiseuille flow decays as $\exp(-2.405x)$, and that, for uniform entry flow, the flow was within 1% of Poiseuille flow at $x = 1.3$. Also, Dagan *et al.* (1982) solved a problem similar to A and found that the flow was within 1.5% of Poiseuille flow at $x = 0.5$. Further, experimentation showed that extending the calculation region beyond $x = 4$ did not make a significant difference to the numerical results, nor did varying the condition applied at $x_{\max} = 4$ (e.g. using a symmetry condition).

The zero-suction problem C is more difficult, in that there is no dominant term that is independent of x for large x. As $x \to \infty$, the flow has the form of a series of counter-rotating eddies, all of the same size but decaying exponentially in magnitude – see Appendix A below for details. This asymptotic structure was used to set the values at $x_{\max} = 8$ by locating an eddy centre in the numerical results and scaling the asymptotic solution so that the vorticity from both solutions is the same at the eddy centre. Comparison showed that the numerical solution converges towards the asymptotic solution as the grid is refined. Two further configurations were tried – a solid wall, and symmetry, at $x_{\max} = 4$. The values obtained at the entrance to the side branch did not depend signficantly on the method used at $x = x_{\max}$. This is not surprising in the light of the strong decay implied by the asymptotic solution (see Appendix A). In the results presented below, a solid wall was used for Problem C.

3.4. *The iteration procedure*

The Gauss–Seidel method was used to solve the system of finite-difference equations. Each complete sweep through the grid was split into a sweep on velocity followed by a sweep on vorticity, so that all the velocity values were updated before the vorticity was calculated. This ensured that the values used to approximate the derivatives

h	ψ	ζ	h	ψ_e	ζ_e
$\frac{1}{16}$	0.92703	7.0824	$\frac{1}{16}$ & $\frac{1}{32}$	0.94124	8.5527
$\frac{1}{32}$	0.93769	8.1851	$\frac{1}{16}$ & $\frac{1}{64}$	0.94464	9.0025
$\frac{1}{64}$	0.94354	8.8825	$\frac{1}{32}$ & $\frac{1}{64}$	0.94549	9.1150

TABLE 2. Values from the axisymmetric problem A at $(x, r) = (-\frac{1}{16}, \frac{15}{16})$. ψ_e and ζ_e were obtained using h^2-extrapolation.

appearing in the forcing terms $\boldsymbol{G}$ in (2.11) all came from the same iteration (mixing values from different iterations slows down the rate of convergence). The most straightforward ordering was used for the sweep through the grid, i.e. an inner loop with $j(r)$ increasing, and an outer loop with $i(x)$ increasing. Various other strategies were tested, but there was little difference in the convergence rate. The wall vorticity and main-tube far-field velocity and vorticity were calculated at the start of each sweep. Equation (3.2) was solved every sweep.

The convergence test was based on the velocity integrals (2.14f) and (2.17g), with the iteration continued until these quantities were constant to at least six signficant figures. Checks on absolute and relative changes to the dependent variables showed this to be adequate.

3.5. *Accuracy*

All the finite-difference equations have truncation error $O(h^2)$, and once solutions were found on successive grids (e.g. $M_0 = 16$ and 32), h^2-extrapolation was used in an attempt to improve the results (this is discussed further below).

Consider the axisymmetric problem A. It can be recast in stream function–vorticity terms, and solved in standard fashion. This was done, using the Woods (1954) formula for the boundary vorticity. Good agreement was found for the results obtained from the stream function–vorticity and velocity–vorticity calculations. In particular, for the extrapolated results with $M_0 = 32$ and 64, graphically identical streamline patterns were obtained. Further, the streamline patterns from the stream function–vorticity method with $M_0 = 16$ and 32 and $M_0 = 32$ and 64 were also identical, although this was not true for the velocity–vorticity results. Hence the stream-function–vorticity method is more accurate than the velocity–vorticity method.

It is not immediately apparent that h^2-extrapolation is useful in a problem with a singularity. Using the results from the stream function–vorticity calculation on the three grids ($M_0 = 16$, 32 and 64), the behaviour of the numerical solution was investigated. Over most of the grid, the difference between the values from the different grids was broadly consistent with an h^2 error, although the variation was small and the extrapolation process had little effect. However, the behaviour cannot be said to be h^2 at points strongly influenced by the corner singularity. In table 2, values are given for a point near the corner where the largest variation between the grids was found. Also given are various extrapolated values. There is a consistent trend in the values as the grid is refined, and the extrapolation process appears to improve the results. This was true throughout the grid, and the values used below are the extrapolated values from the stream function–vorticity method with $M_0 = 32$ and 64. Note however, that the same flow pattern would be obtained, and the same conclusions would be reached, if the finest-grid solution was used instead of the extrapolated values.

Dagan *et al.* (1982) have solved a similar axisymmetric problem, using an infinite-series method. In their problem, the matching condition down the side tube, (2.12*c*), was replaced by a symmetry condition. Excellent agreement was found between their results and values obtained from our present stream function–vorticity method with the same symmetry condition (indeed the agreement was also excellent with the values obtained by (2.12*c*) – the symmetry condition having no effect on the results obtained in the main tube).

For Problem C, we have no other numerical solution with which to compare our results. However, our solution is physically sensible, and shows excellent qualitative agreement with solutions of the analogous two-dimensional problem (see in particular Higdon 1985), and experimental studies (Taneda 1979; Shen & Floryan 1985). Also, main-tube test calculations with the velocity specified on $x = 0$ gave satisfactory results with the grids used here. The tests included problems with discontinuous, but not singular, wall shear. A further test, using the eddy solution given in Appendix A, gave excellent results. The solution used below for Problem C is the h^2-extrapolation from $M_0 = 32$ and 64.

Finally, the pressure and shear values shown in the plots below are those obtained from the integral solution (2.5*a*, *b*) for the flow in the main tube. These shear values were used as they showed a smaller variation with the grid step than the values given directly by the numerical solution, although the results presented below would not be affected significantly if the latter were used. The two sets of shear values were converging with decreasing step size.

4. Results

In this section the results of the study are presented; first, the axisymmetric solution (A); second, the zero-suction component (C); and third, flows given by a combination of the two (Q_b A + C). Finally, the entrainment region of the fluid sucked into the side branch from the main tube is considered. Below, upstream or downstream of the side-branch entrance will refer to the region in the main tube with $r > 1$ and $y < 0$ or $y > 0$, respectively.

4.1. *The axisymmetric problem*

Figure 3 gives the flow for an incompressible fluid being slowly sucked down a circular pipe from a semi-infinite region, i.e. the solution to the problem formed by (2.11)–(2.14). It contains the streamlines, the velocity at the side-branch entrance, and the wall shear stress τ_y and pressure on the walls of the main tube. Sampson (1891) derived an analytic solution for the Stokes flow through a circular hole in a wall of zero thickness (this solution can be found in a more accessible form in de Mestre & Guiney 1971). Except near the entrance the streamlines in Problem A are graphically indentical with those in Sampson's solution, or indeed its limit form – the flow generated by a point sink at the origin, as given by the leading term of (2.14*d*, *e*). Unlike Sampson's solution, the present solution has a non-zero transverse velocity at the entrance, and hence non-zero wall shear. As noted by Dagan *et al.* (1982), the axial velocity at the entrance to the side branch ($u_0(0, r)$) lies between that of Sampson and Poiseuille flow, and there is a short entrance length (u_0 is within 1 % of Poiseuille flow at $x = 0.6$). Compared with Poiseuille flow, $u_0(0, r)$ is smaller in the centre of the tube and greater near the walls. Both the pressure and the shear stress on the walls of the main tube show a singularity as $r \to 1+$, as expected.

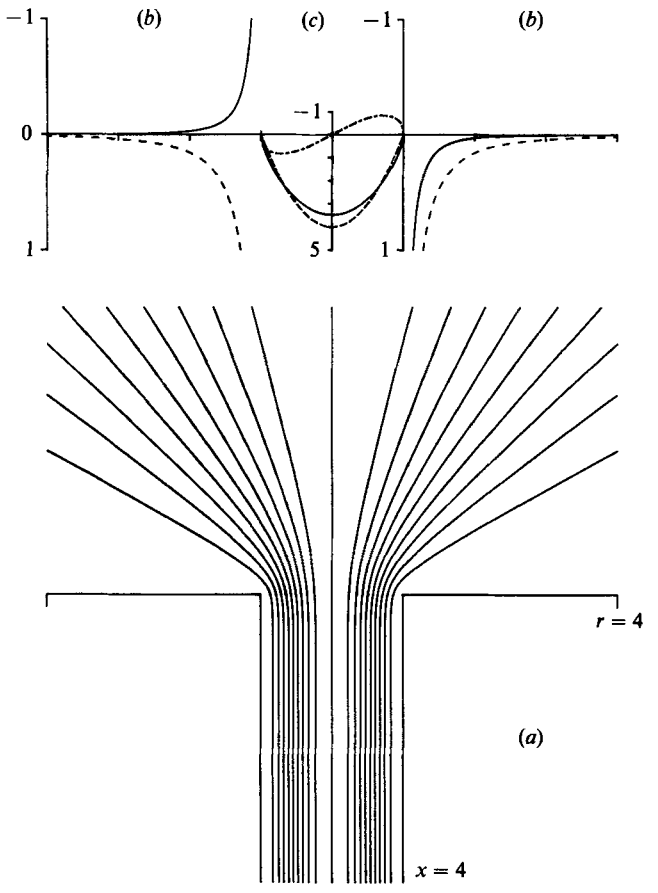

FIGURE 3. Axisymmetric solution A: (*a*) evenly spaced streamlines; (*b*) main-tube wall shear stress τ_y (——) and pressure p (– – – –) (*c*) velocity on the side-branch entrance ($x = 0$): ——, u_x; –·–, $u_y \times 2$; – – – –, Poiseuille flow.

4.2. *The zero-suction component*

As noted above, this the very slow shear flow of an incompressible fluid along a flat wall with an semi-infinite circular pipe set perpendicularly into the wall (see figure 1), the governing equations being (2.11) and (2.15)–(2.17). The flow along the plane of symmetry ($z = 0$) is shown in figure 4, which gives particle paths (streamlines), the velocity components at the mouth to the side branch, and the shear stress (τ_y) and pressure on the walls of the main tube. The pressure on the wall is small compared with that generated by the axisymmetric component of flow, a consequence of weakness of the normal velocity (u_1) at $x = 0$.

Also clear from figure 4 is the position of the dividing streamline between the outer flow (essentially that past the side branch) and the inner flow in the side branch. As for the analogous two-dimensional shear flow past a slot (Takematsu 1966), the separation and reattachment of the flow occur on the side-branch wall, and the outer flow penetrates a considerable depth into the side branch. (Indeed, it follows from the Stokes expansion (Moffatt 1964) that, unless the flow is symmetric at the corner, it cannot separate from the corner (Takematsu 1966; Weinbaum 1968).) The present calculations give the separation (and reattachment) point as $x_s = 0.08$, and the depth

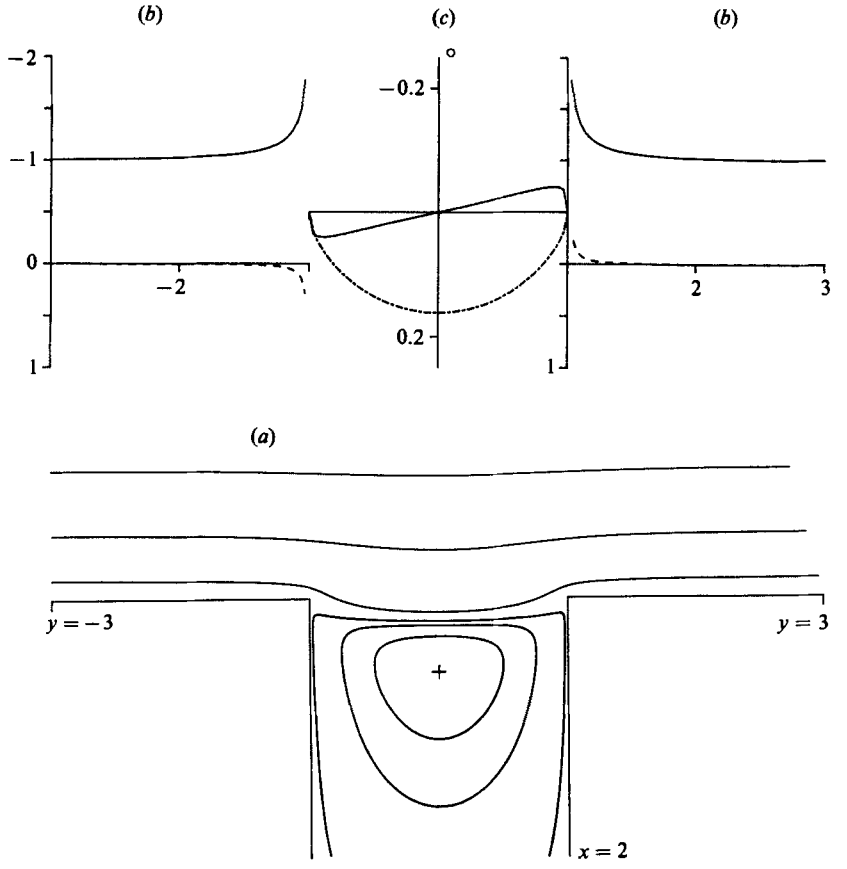

FIGURE 4. Zero-suction solution C: (*a*) streamlines (+ denotes the centre of an eddy); (*b*) main-tube wall shear stress τ_y (——) and pressure p (– – – –); (*c*) velocity on the side-branch entrance ($x = 0$): ——, u_x: – · –, u_y.

of the dividing streamline on $r = 0$ as $x_d = 0.174$. Because of the effect of the corner singularity on the calculation procedure, the former value is a reasonable but not particularly accurate estimate of x_s. For comparison, Takematsu (1966) gives $x_s = 0.035$ for the two-dimensional problem, but this must be regarded as a crude estimate since he uses only four terms of his series solution. Weinbaum (1968) has shown that separation/attachment near a sharp 90° corner occurs at an angle of approximately 41.2° (see figure 6). This point is discussed further below, but, encouragingly, the separation/attachment angle found from our numerical solution for Problem C shows excellent agreement with Weinbaum's value.

The perturbation to the flow in the main tube on the plane of symmetry is small except in the immediate vicinity of the side-branch entrance, while in the side branch the flow beneath the dividing streamline takes the form of a sequence of large asymmetric eddies of decreasing strength (see figure 4 and Appendix B). As mentioned in §3 above, three different sets of boundary conditions were used at $x = x_{max}$ in place of (2.17*c*). With $x_{max} = 4$, the solid wall and the symmetry condition gave essentially the same results – a large clockwise-rotating eddy, with a smaller eddy, rotating slowly in an anticlockwise sense, beneath it. This is the same pattern as that found by Higdon (1985) for the two-dimensional problem with the same

aspect ratio. Using the asymptotic solution to set the values at $x_{\max} = 8$ produced a sequence of eddies decaying in strength, as predicted.

The discussion of the solution for C above is concerned with the flow in the plane of symmetry. However, the flow is similar for non-zero z with $z < 1$. In particular, except immediately near the corner (i.e. $|1-r| \ll 1$) the flow is largely two-dimensional with u_z much smaller than u_y (this follows from the solution, which has $v_1 \approx -w_1$ over most of the domain). The surface dividing the inner and outer flows is obtained by rotating the dividing streamline suggested by figure 4. For the outer flow, particle paths with $z \neq 0$ are similar to those with $z = 0$, with some, though not much, movement towards (in $y < 0$) and then away from (in $y > 0$) the plane of symmetry. In the large eddies below the dividing surface, particles traverse simple orbits similar to those shown in figure 4, with little movement in the transverse direction (this is as predicted by the asymptotic solution given in Appendix A). A good idea of the values of u_y on the side-branch entrance, and the wall shear stress τ_y, for non-zero z, is obtained by rotating the solutions given in figure 4, although τ_y has a weaker singularity on $y = 0$ ($O((1-r)^{-\frac{1}{3}})$) than on $z = 0$ ($O((1-r)^{-0.456})$). Further, for any particular value of r, both the wall shear stress (τ and τ_y) and the pressure have maximum magnitude on the line of symmetry ($z = 0$ or $\theta = 0, \pi; r > 1$), with the shear taking its minimum magnitude on $y = 0$ ($\theta = \pm\frac{1}{2}\pi; r > 1$) and the pressure dropping to zero there. Indeed, the pressure, u_x and u_r are zero at $y = 0$ for all x and z, as can be seen from (2.10).

4.3. *Composite flows*

We shall now consider linear combinations of the two basic flows described above. In general, adding a multiple ($Q_b > 0$) of Problem A to Problem C gives, in comparison to C alone, an increase in the magnitude of the pressure and the shear on the wall of the main tube upstream of the side branch. It follows that there are no stagnation points on the main-tube wall in this region. Further, with $Q_b > 0$, the magnitudes of the pressure and shear on the main-tube wall are greater upstream than downstream of the side branch (comparing the points $(0, y, z)$ and $(0, -y, z)$ with $r > 1$). Indeed, if Q_b is sufficiently large (see below), there will be a stagnation point on the main-tube wall downstream of the side branch. Note that a true stagnation point (i.e. with τ zero) can occur only on the line of symmetry, although a particular component of the shear may be zero for non-zero z – e.g. τ_y in $y > 0$.

Because of the fast exponential decay in the strength of C in the side branch, all except the eddy closest to the entrance will be suppressed with a small but finite Q_b (10^{-3} say). Consider $Q_b = 1/200$. This leaves the strongest eddy intact, but considerably reduced in size and strength, and compressed onto the upstream wall of the side branch (figure 5). The fluid sucked into the side branch from the main tube passes over the top of the eddy, between it and the downstream wall of the side branch, then spreads out to occupy all of the side branch below the eddy.

With $Q_b = 1/200$, as well as the flow separation and reattachment on the upstream wall of the side branch due to the eddy, there is a stagnation point on the downstream wall, where the flow along the main tube and that down the side branch divide. Compared with Problem C, the separation at the top of the eddy is now further down the wall, and the stagnation point on the downstream wall is closer to the entrance. As Q_b is increased from 1/200 the eddy remains on the upstream wall, but decreases in strength and size until at $Q_b = 0.027$ it is suppressed completely by the flow into the side branch. For all $Q_b \geqslant 0.027$ the flow remains attached to the upstream wall of the side branch.

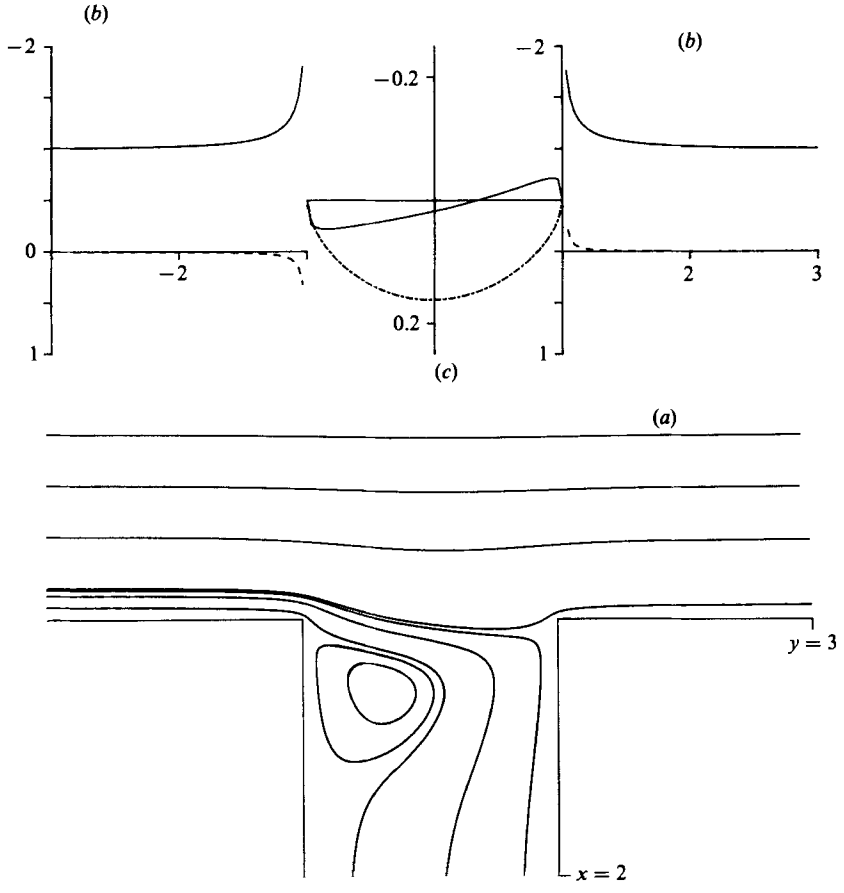

FIGURE 5. $Q_b = 1/200$ (see figure 4 for description).

On the downstream side-branch wall, as Q_b is increased from zero the stagnation point moves closer to the entrance, until for $Q_b = Q_{bc}$, it is on the corner $\boldsymbol{x} = (0,1,0)$. The three-dimensional flow near a sharp edge is analysed in Appendix B, from which it follows that:

$$\tau_r \sim (Q_b A_0 + A_1 \cos\theta)\,\sigma^{-0.456} + (Q_b B_0 + B_1 \cos\theta)\,\sigma^{-0.091}, \tag{4.1a}$$

$$\tau_\theta \sim C_1 \sigma^{-\frac{1}{3}} \sin\theta, \tag{4.1b}$$

on the main-tube wall near the side branch, where $\sigma = r-1$, $0 < \sigma \ll 1$, and A_0, A_1, B_0, B_1, and C_1 are constants. Further, the terms given in (4.1) are the only terms in the Stokes expansions that give non-zero wall shear as $\sigma \to 0$. The terms of $O(\sigma^{-0.456})$ and $O(\sigma^{-0.091})$ in (4.1*a*) arise from components of flow in a plane normal to the walls which are, respectively, asymmetric and symmetric about the corner, while (4.1*b*) is due to the flow along the edge. Inspection of the solutions, or physical reasoning, shows that $A_0 > 0$ $A_1 < 0$ and $C_1 > 0$. Weinbaum (1968) studied the two-dimensional flow that gives (4.1*a*), and showed that the corner is a separation/stagnation point only if the flow is symmetric about the corner. Hence, from (4.1*a*)

$$Q_{bc} = -\frac{A_1}{A_0}. \tag{4.2}$$

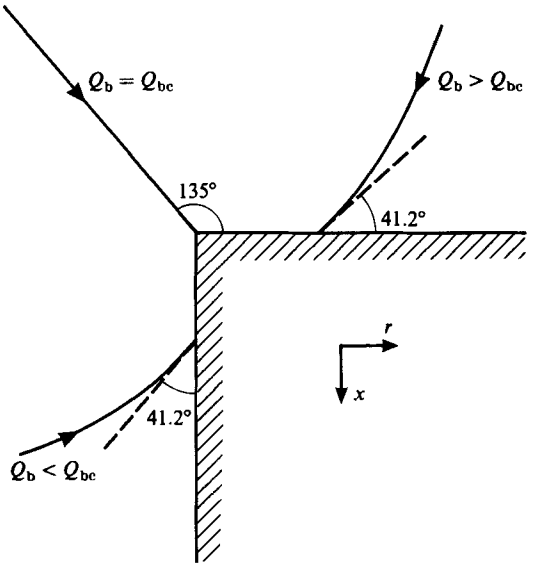

FIGURE 6. Dividing streamline in the plane of symmetry ($z = 0$) for $Q_b \approx Q_{bc}$.

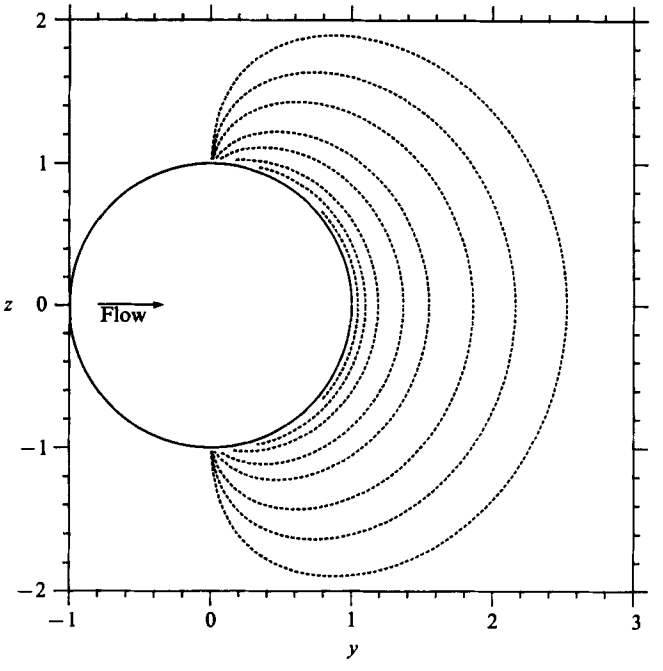

FIGURE 7. Contours of zero wall shear stress (τ_y). From the centre, these have $Q_b = \frac{1}{2}$, 1, 2, 5, 10, 25, 50 and 100.

Weinbaum (1968) also showed that if the flow in the plane normal to the walls is asymmetric with respect to the corner, separation/stagnation occurs away from the corner (approaching the corner asymptotically as the asymmetric component of flow tends to zero) with a constant separation angle of 41.2° approximately. Hence the flow behaves discontinuously with respect to Q_b; for $0 < Q_{bc} - Q_b \ll 1$ the stagnation

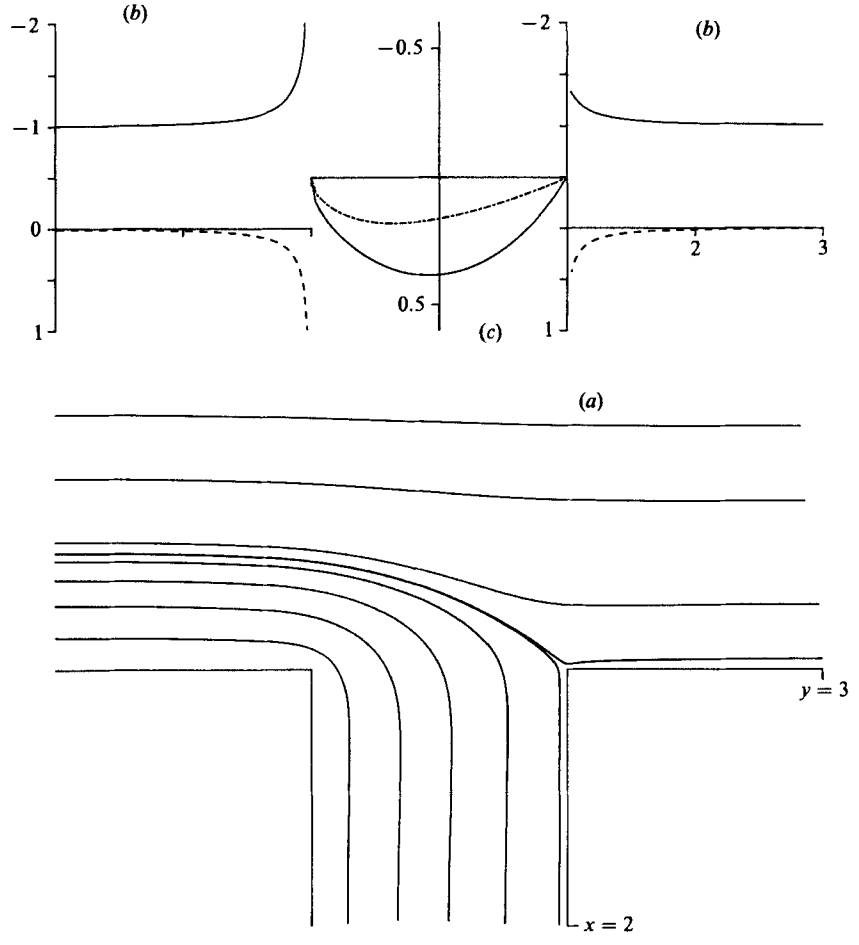

FIGURE 8. $Q_b = 0.11$ (see figure 4 for description).

point on $z = 0$ occurs on the side-branch wall near the corner with an attachment angle of 41.2°; when $Q_b = Q_{bc}$ the flow is symmetric about the corner with the stagnation point on the corner; and if $0 < Q_b - Q_{bc} \ll 1$ the stagnation point is on the main-tube wall, again with an attachment angle of 41.2° (see figure 6). The effect of this discontinuity can also be seen in the main-tube wall shear. Suppose $\theta = 0$ and $\sigma \to 0+$. Then, for all $Q_b < Q_{bc}$, $\tau_r \to -\infty$ as $\sigma^{-0.456}$. If $Q_b = Q_{bc}$, $\tau_r \to -\infty$ again, but as $\sigma^{-0.091}$, while if $Q_b > Q_{bc}$, $\tau_r \to +\infty$ as $\sigma^{-0.456}$.

If $Q_b = 0$, it follows from (4.1) that the flow in the main tube is towards the side branch at the upstream edge, and away from it at the downstream edge, as might be expected. Suppose now that $0 < Q_b \leqslant Q_{bc}$. Then the region in which flow at the edge is away from the side branch is reduced to $-\theta_s \lesssim \theta \lesssim \theta_s$, where $\theta_s = \cos^{-1}(Q_b/Q_{bc})$, with flow towards the edge elsewhere. This implies that there are two regions with backflow ($-\frac{1}{2}\pi < \theta \lesssim -\theta_s$ and $\theta_s \lesssim \theta < \frac{1}{2}\pi$), in which $\tau_y > 0$ and the flow in the main tube near the downstream edge of the side branch is towards the side branch. As $Q_b \to Q_{bc}$, $\theta_s \to 0$ and the portion of the downstream edge of the side-branch entrance in which the flow is from the side branch into the main tube disappears in the limit. For $Q_b > Q_{bc}$, $\tau_r > 0$ for all θ, and there is backflow everywhere at the downstream edge in the main tube. As Q_b increases, the region with backflow grows, but never

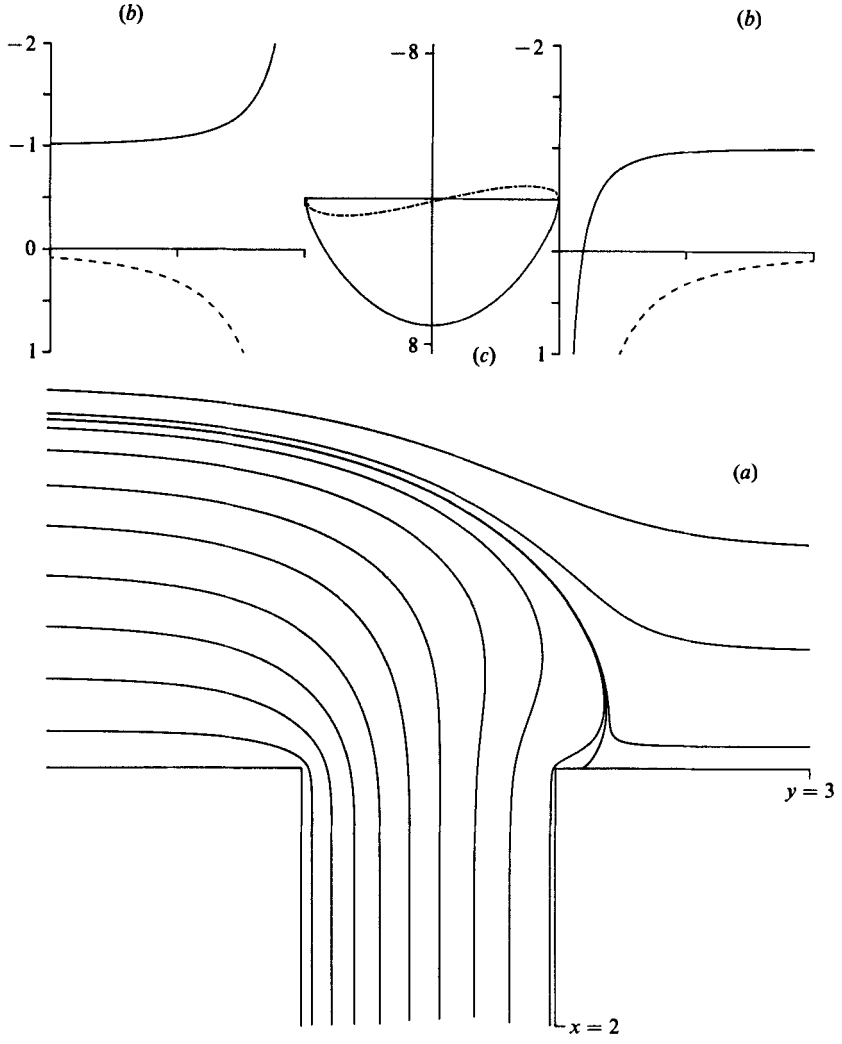

FIGURE 9. $Q_b = 2$ (see figure 4 for description).

extends into $y \leqslant 0$ (for $0 < \sigma \ll 1$ this can be seen from (4.1), and for other $r > 1$ it can be deduced from the Fourier decomposition (2.10) and physical arguements). Figure 7 shows the region for which $\tau_y > 0$ for various $Q_b > Q_{bc}$.

Also of interest is the behaviour of the total wall shear near the side-branch entrance. From (4.1):

$$\tau \sim |Q_b A_0 + A_1 \cos\theta| \, \sigma^{-0.456} \quad \text{as } \sigma \to 0,$$

except at $\theta = \pm\theta_s$ if $Q_b < Q_{bc}$, where $\tau \sim C_1 \sigma^{-\frac{1}{3}} |\sin\theta|$. Thus, if $Q_b < Q_{bc}$, τ will be least near $\theta = \pm\theta_s$, with its maximum at $\theta = \pi$ and a local maximum at $\theta = 0$. If $Q_b \geqslant Q_{bc}$, τ will take its maximum at $\theta = \pi$ and its mimimum at $\theta = 0$.

The behaviour of the pressure p on the main-tube wall as $\sigma \to 0$ is

$$p \sim 1.8464(Q_b A_0 + A_1 \cos\theta)\sigma^{-0.456} - 4.5922(Q_b B_0 + B_1 \cos\theta)\sigma^{-0.091}. \tag{4.3}$$

Note that the flow *along* the edge does not give a singular term in the pressure (see Appendix B). For $Q_b = 0$ the wall pressure in the main tube is increased at the upstream edge of the side-branch entrance, and decreased at the downstream edge.

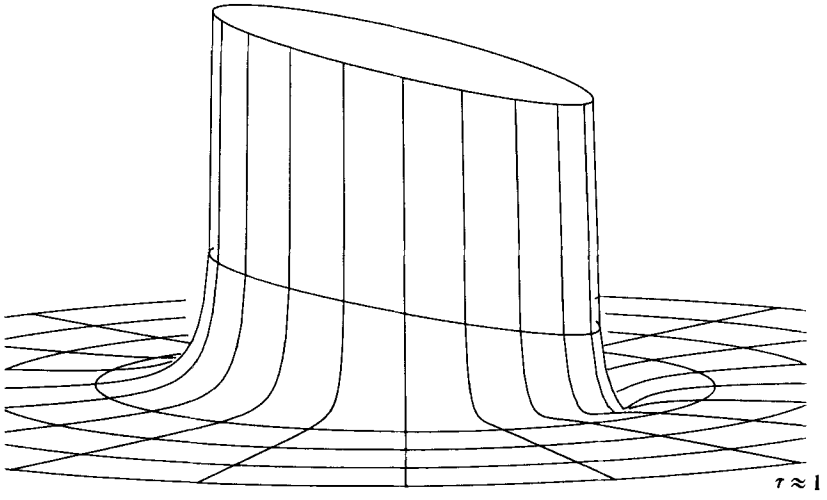

FIGURE 10. Total wall shear stress τ for $Q_b = 2$.

If $0 < Q_b < Q_{bc}$, the pressure is reduced for $-\theta_s \lesssim \theta \lesssim \theta_s$, and increased elsewhere, while if $Q_b \geqslant Q_{bc}$, the edge pressure is increased for all θ, but has its minimum at $\theta = 0$ and its maximum at $\theta = \pi$ (see figures 4, 5, 8 and 9).

Equation (4.2) and, separately, the wall shear or the velocity from the numerical solutions can be used to estimate Q_{bc}. Both gave $Q_{bc} \approx 0.11$. Figure 8 shows particle paths, etc., in the plane of symmetry for $Q_b = 0.11$. Note in particular the weak singular behaviour of the shear and pressure on the downstream wall, as predicted by (4.1*a*) and (4.3).

The velocity on the mouth of the side branch is greatly dependent on the value of Q_b. For Problem C, u_x is antisymmetric and u_y symmetric with respect to y on $x = 0$, $r < 1$, while the opposite is true for Problem A. As Q_b is increased from zero, the original symmetry is disturbed, until at $Q_b = Q_{bc}$ both u_x and u_y are positive everywhere on the side-branch entrance (see figures 4, 5 and 8).

Suppose now that $Q_b > Q_{bc}$. As Q_b is increased the stagnation point on the downstream wall of the main tube moves downstream (see figure 7), and the flow at the entrance to the side branch is increasingly dominated by the axisymmetric component of flow A. For example, when $Q_b = 2$, the velocity components at the entrance are close to those from A, and the pressure on the main-tube wall is dominated by that from A, even at a considerable distance from the entrance (see figures 3 and 9). The latter is not surprising in view of the dependence of the wall pressure on u_x (§2). Also shown in figure 9 is the dividing streamline in the plane of symmetry $z = 0$. This streamline, which separates the fluid going along the main tube from that going down the side branch, makes an acute angle with the wall downstream of the stagnation point, with the fluid particles turning back towards the stagnation point. Weinbaum's (1968) results (see figure 6) and the present numerical solutions shows that this angle is acute for all $Q_b > Q_{bc}$. Figure 10 is a surface plot of the total wall shear stress τ for $Q_b = 2$. The dominant effect of the corner singularity on the wall shear stress near the side-branch entrance can be seen clearly. In general, the wall shear varies significantly from its incoming value of unity only in a region close to the entrance, except for large Q_b. Note also the dip in τ near the stagnation point downstream of the entrance.

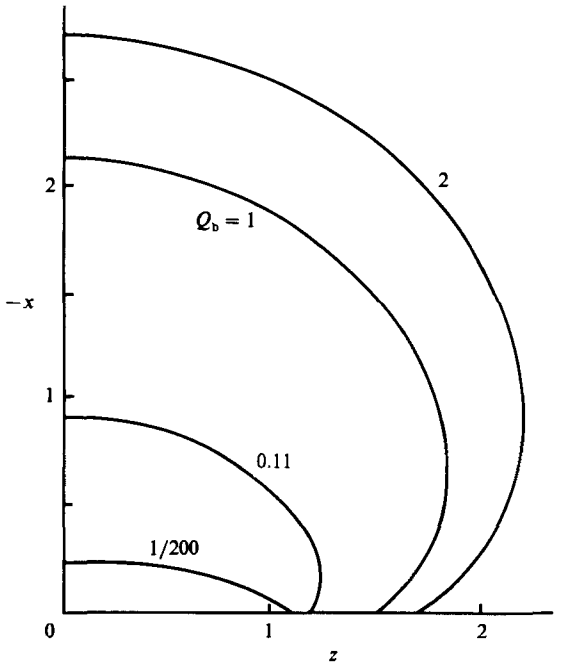

FIGURE 11. Entrainment region at $y = -3$.

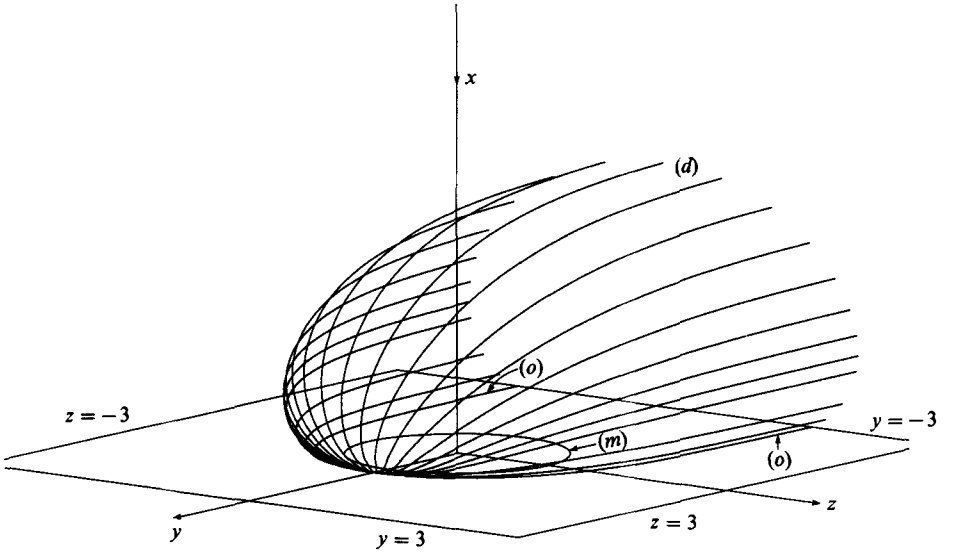

FIGURE 12. Dividing streamlines for $Q_b = 2$. The particle path (d) lies in the plane of symmetry ($z = 0$), (o) is at the main tube wall, while (m) is the side-branch entrance ($r = 1$ on $x = 0$).

4.4. *The entrainment region*

Of interest in this problem is the entrainment region, i.e. the region in the main tube occupied by fluid which is eventually sucked down the side branch. This was established by calculating particle paths. Figure 11 shows the results for various Q_b at $y = -3$, where the flow is close to the incoming shear flow. Figure 12 shows the dividing streamlines for $Q_b = 2$.

5. Discussion

First, we note that although the analysis above is in terms of a suction problem with the flow down the side branch, a change of sign gives the solution for the injection problem with the main-tube shear flow in the opposite direction. Also, instead of fixing the basic shear rate in the main tube and varying the flow rate in the side branch, we could do the reverse, i.e. the results given in §4 above also describe flows with a far-field shear rate in the main tube of Q_b^{-1} and a volume flow of 2π in the side branch. For example, with the appropriate rescaling, figure 5, which has $Q_b = 1/200$, gives the solution for a flow with a high shear in the main tube.

Consider the solutions as presented with a suction flow. Except near the entrance to the side branch, the axisymmetric flow A is close to Sampson's (1891) solution in the main tube, and to Poiseuille flow in the side branch. At the entrance, the streamlines in Problem A have moved out from the axis compared to those in Poiseuille flow. The flow with an incoming linear shear in the main tube and zero net flow into the side branch (Problem C) is, except in the immediate neighbourhood of the entrance, essentially two-dimensional, with the outer flow penetrating into the side branch and generating a sequence of counter-rotating eddies which decrease rapidly in strength. For composite flows (Q_b A + C) we have found a complex pattern of behaviour for small side-branch flow rates. For $Q_b < 0.027$ there is at least one three-dimensional eddy in the side branch, while for $Q_b > Q_{bc} \approx 0.11$, the flow in the side branch is unidirectional. For $0 < Q_b < Q_{bc}$, the corner singularity implies regions of both forward and reversed flow, and an associated decrease or increase in the pressure, at the downstream edge of the side-branch entrance, as detailed in §4 above. For $Q_b > Q_{bc}$, there is an increase in the pressure near both the upstream and downstream edge, while for Q_b of $O(1)$, the flow near the entrance is dominated by the axisymmetric component of the flow (Problem A), and in the far field by the main-tube shear flow. Owing to the weakness of u_x at the mouth in Problem C, the contribution from A to the pressure on the main-tube wall is dominant for r of $O(1)$, except for very small side-branch flow rates.

Consider now the physiological problem that motivated this study. Before drawing any conclusions we should examine the applicability of our model to the experimental conditions. A basic complication arises from the fact that blood is not a homogeneous Newtonian fluid. While the non-Newtonian behaviour is insignificant at a sufficiently high shear rate (see Caro *et al.* 1978, p. 176), it may become important near a stagnation point. This aspect is beyond the scope of the present study.

Our idealized problem was formulated by assuming that the flow in the main tube is steady and fully developed. This is not the situation in the thoracic aorta, where the flow is periodic with little or no net flow for more half the flow cycle. Following this resting phase there is a pressure pulse, with flow undergoing a rapid acceleration followed by a rapid deceleration. There is likely to be a period of relatively weak reversed flow before the net flow ceases (see Pedley 1980, p. 40). The Wormersley parameter α is defined as $\alpha = a^*(\rho\omega/\mu)^{\frac{1}{2}}$, where ω is the angular frequency of the flow. If α is large, the flow can be analysed in terms of an inviscid core flow with a Stokes layer of thickness $4a^*/\alpha$ at the wall (details can be found in Pedley 1980).

In a fully grown rabbit, representative values for the thoracic aorta are $U^* = 60$, $a^* = 0.16$, $b^* = 0.016$, and $\mu/\rho = 0.04$, all in c.g.s. units, where U^* is the peak value (McDonald 1974; CR). Estimates for the heart rate vary from 200 to 300 beats/min. Taking 240 as a characteristic value gives $\omega = 8\pi$ for the fundamental frequency. Hence, $\alpha \approx 4$, and we cannot assume an inviscid core flow with a distinct boundary

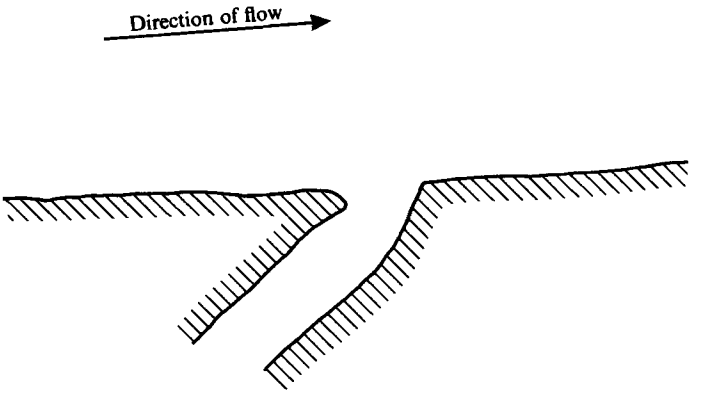

FIGURE 13. The cross-section of a branch formed by an intercostal artery and the thoracic aorta in a rabbit (taken from a photograph supplied by R. Kratky).

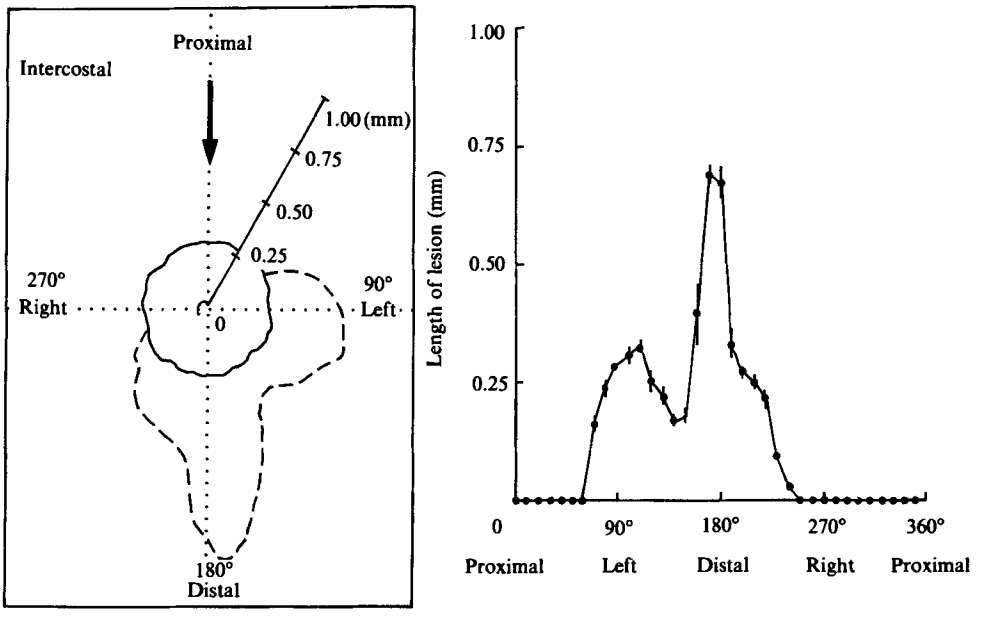

FIGURE 14. Prelesion at an intercostal orifice (after Cornhill & Roach 1976). The flow is from proximal to distal.

layer (cf. Sobey 1977). Near the entrance to an intercostal artery, the relevant lengthscales are given by the dimensions of the entrance. Non-dimensionalizing as in §2, we obtain a peak main-tube Reynolds number of 240, and since $\delta = \frac{1}{10}$, $Re_s = 2.4$. If we now assume that the characteristic time is the same as in the core, i.e. ω^{-1}, and define the local Strouhal number as $St = \omega b^*/\delta U^*$, then $St \approx 0.067$, and $Re_s St \approx 0.16$.

Therefore, as a first approximation, it appears reasonable to ignore the unsteady terms in the Navier–Stokes equations and the effect of the curvature of the wall of the thoracic aorta. However, inertia is not negligible as Re_s is $O(1)$. Dropping the unsteady terms allows a quasi-steady analysis, and hence the use of the Stokes equations for a large part of the flow cycle, in particular, suitably scaled high-Q_b solutions. Unfortunately, the above Stokes analysis may not give accurate results for the peak flow rates.

In our model we have also assumed that the side branch is perpendicular to the main tube. The cross-section of a typical intercostal-aortic branch is shown in figure 13, from which it is clear that our assumed geometry is not realistic, although it is an obvious first step. The question of a realistic geometry for a model problem is further complicated by the flexibility of blood vessels – the cross-sectional area of an artery can vary by around 20% during a flow cycle. Moreover, high shear stresses and pressure might induce a considerably larger variation near a branch. There will, however, be a stagnation point somewhere on the downstream wall, and our solutions suggest that its position – i.e. whether it occurs on the main-tube or side-branch wall – is important.

Figure 14 shows results obtained by CR for a particular intercostal orifice. Note that the prelesion area is maximum downstream, and does not extend upstream, although atherosclerosis may appear all around the ostium later (Nerem & Levesque 1983). Our results, while valid for the particular problem considered, can only be interpreted in a qualitative manner with respect to the physiological problem. However, in the light of CR's results (and others – see Chobanian 1983), they are consistent with, and offer support for, the low-shear hypothesis outlined in § 1 above.

This study was funded by SERC, under a grant obtained by Dr T. J. Pedley, to whom the author is indebted for many useful discussions. The author is also grateful to Professor S. C. R. Dennis for discussions on the numerical aspects, and, on the physiological aspects, Dr Margot Roach, Ralph Kratky, and their colleagues at the University of Western Ontario. Thanks are also due to the referees for their helpful suggestions, particularly for bringing recent developments in research in atherosclerosis to the attention of the author.

Appendix A. The asymptotic structure in the side branch

In §2 the zero-suction component of the flow in the side branch is required to decay to zero as $x \to \infty$. Here, we derive the details of this decay. For the analogous two-dimensional channel, Moffatt (1964) demonstrates that the flow takes the form of a series of counter-rotating eddies, all of the same length but with magnitude decaying exponentially in x, and we might expect a similar structure for the present problem.

It is convenient at this stage to use Helmholtz's theorem to introduce a vector potential, i.e. a vector $\boldsymbol{\psi} = (\psi_x, \psi_r, \psi_\theta)$ in (x, r, θ) such that

$$\boldsymbol{u} = \boldsymbol{\nabla} \times \boldsymbol{\psi}, \tag{A 1}$$

where, since $\boldsymbol{u} = (u_x, u_r, u_\theta)$ is soleniodal, $\boldsymbol{\psi}$ can also be made solenoidal. The equations of motion now become

$$\nabla^2 \boldsymbol{\psi} = -\boldsymbol{\zeta}, \tag{A 2}$$

and

$$\nabla^2 \boldsymbol{\zeta} = 0, \tag{A 3}$$

where $\boldsymbol{\zeta} = (\zeta_x, \zeta_r, \zeta_\theta)$ is the vorticity vector.

The boundary conditions are:

$$\psi_x = \psi_\theta = u_x = u_\theta = 0 \quad \text{at } r = 1 \tag{A 4}$$

plus a boundedness condition at $r = 0$. Note that (A4) ensures that $u_r = \zeta_r = 0$ at $r = 1$.

Re(k)	Im(k)
2.5678	1.1226
5.3172	0
6.0038	1.6081
8.5330	0
9.2322	1.8169
11.705	0
12.417	1.9613
14.863	0
15.586	2.0726
18.015	0

TABLE 3. Eigenvalues k from (A 11) in order of increasing real part

Assuming a separable solution, we find that the vector potential, velocity and vorticity can be written as

$$\boldsymbol{\psi} = \mathrm{e}^{-kx}(\Psi_x(r)\sin\theta, \Psi_r(r)\sin\theta, \Psi_\theta(r)\cos\theta), \tag{A 5}$$

$$\boldsymbol{u} = \mathrm{e}^{-kx}(U_x(r)\cos\theta, U_r(r)\cos\theta, U_\theta(r)\sin\theta), \tag{A 6}$$

and

$$\boldsymbol{\zeta} = \mathrm{e}^{-kx}(\Gamma_x(r)\sin\theta, \Gamma_r(r)\sin\theta, \Gamma_\theta(r)\cos\theta). \tag{A 7}$$

With (A 7) it is easily shown that the bounded solenoidal solution of (A 3) is:

$$\Gamma_x = cJ_1(kr), \tag{A 8a}$$

$$\Gamma_r = aJ_0(kr) + (a+c)J_2(kr), \tag{A 8b}$$

$$\Gamma_\theta = aJ_0(kr) - (a+c)J_2(kr) \tag{A 8c}$$

where a and c are constants, and J_n is the Bessel function of the first kind of order n. Equations (A 2), (A 7) and (A 8) now yield

$$\Psi_x = AJ_1(kr) + \frac{c}{2k}rJ_0(kr), \tag{A 9a}$$

$$\Psi_r = BJ_0(kr) + \left[A + B - \frac{1}{k^2}(a+c)\right]J_2(kr) + \frac{c}{2k}rJ_1(kr), \tag{A 9b}$$

$$\Psi_\theta = BJ_0(kr) - \left[A + B - \frac{1}{k^2}(a+c)\right]J_2(kr) - \frac{1}{k}\left(a + \frac{c}{2}\right)rJ_1(kr), \tag{A 9c}$$

as the bounded solenoidal solution for $\boldsymbol{\psi}$.

Obtaining $\boldsymbol{u}$ from (A 1) and (A 9), the boundary conditions (A 4) produce

$$a = -\frac{ckJ_2(k)}{2J_1(k)}, \quad A = -\frac{cJ_0(k)}{2kJ_1(k)}, \quad B = \frac{cJ_0(k)J_2(k)}{4J_1^2(k)} \tag{A 10a, b, c}$$

and the eigenrelation

$$k^2J_0^3(k) - kJ_0^2(k)J_1(k) + (k-2)J_0(k)J_1^2(k) - kJ_1^3(k) = 0. \tag{A 11}$$

The first 10 non-trivial solutions of (A 11) that have a positive real part are given in table 3. These solutions alternate between complex and real k, with $k_0 = 2.5678 + 1.226\mathrm{i}$ the most important as it has the smallest real part. Note that no pure imaginary solutions were found for k, i.e. all the separable solutions obtained for

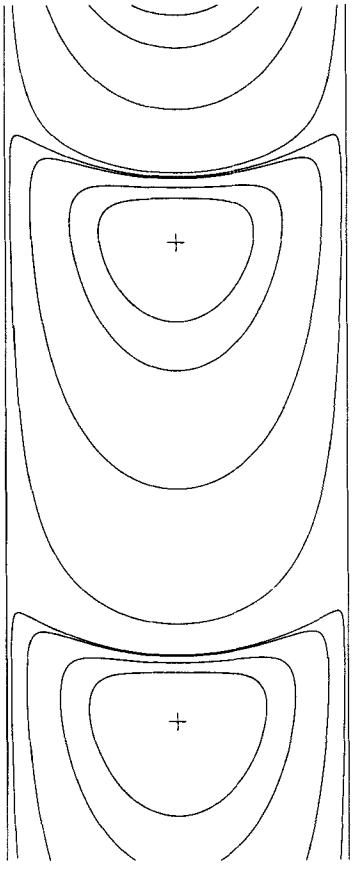

FIGURE 15. Side-branch eddies for $Q_b = 0$ ($z = 0$). +, denotes an eddy centre.

the flow were either exponentially growing or decaying with x, the growing solutions being unacceptable here. For any k satisfying (A 11), both its complex conjugate and $-k$ are also solutions of (A 11).

As is known from the analogous two-dimensional problem (Moffatt 1964), a complex k implies a succession of eddies of the same size, decreasing in magnitude with increasing x. With $k = k_0$, the eddies are 2.798 in length, and the damping factor between successive eddies is 1321. In comparison, Moffatt obtained 2.78 and 350 for these values for the two-dimensional problem. Hence, the two flows have eddies of approximately the same size, but there is a much stronger damping in the three-dimensional case. For all the other complex k given in table 3, as the real part of k increases, so does the complex part. This implies larger, more heavily damped eddies.

The flow pattern in the plane of symmetry ($\theta = 0, \pi$) is shown in figure 15. The eddies show a marked asymmetry, with their centres much closer to the top. This is caused by the rapid decay in magnitude with decreasing x. Reverting to Cartesian coordinates (x, y, z), where the plane of symmetry is given by $z = 0$ as above, the z-component of velocity is given by $e^{-kx}(U_r + U_\theta) \cos\theta \sin\theta$. Inspection of the solution shows that $U_r + U_\theta$ is (relatively) small, and hence that the flow for non-zero z is essentially two-dimensional in character. The orbits of particles off the plane of symmetry (i.e. with z non-zero) are similar to those shown in figure 15.

The angle at which the separation streamline leaves the wall in the plane of symmetry can be determined from the Taylor series for u_x and u_r near the separation point. This is found to be approximately 24.4° (cf. 41.2° for separation near a sharp 270° corner (Weinbaum 1968)).

Finally, we note that an analysis similar to the above can be performed for any of the other Fourier components of the flow.

Appendix B. Steady three-dimensional flow near a sharp corner

In §4 above expansions for the flow near the corner formed by the junction of the main tube and the side branch were employed. These expansions will now be derived. Consider the flow in a domain bounded by two intersecting semi-infinite planes – i.e. the region $-\phi_0 < \phi < \phi_0$, where (z,σ,ϕ) are cylindrical polar coordinates such that the intersection of the planes is given by $\sigma = 0$ (see figure 16). Note that we are interested in the flow near a two-dimensional edge or corner, not a three-dimensional corner (such as the corner of a cube). The flow near a sharp corner is assumed to have a local similarity form, as in Moffatt (1964) and Moffatt & Duffy (1980). Both of these studies concern two-dimensional flow, but in different directions – the former considers the flow in a (σ,ϕ) plane normal to the corner, and the latter the flow in the z-direction along the corner. We shall show that the three-dimensional flow near a sharp edge reduces to two sets of two-dimensional flows which are essentially perpendicular in direction and are generalizations of those of Moffatt (1964) and Moffatt & Duffy (1980).

Sufficiently close to the corner, inertia will be negligible and steady flow will be governed by the Stokes equations. Further, the $\partial^2/\partial z^2$ term in the Laplace operator will not appear at leading order. The boundary conditions are no slip on the walls, i.e.

$$\boldsymbol{u} = (u_z, u_\sigma, u_\phi) = 0 \quad \text{on } \phi = \pm\phi_0. \tag{B 1}$$

It is easily shown that a quasi-two-dimensional flow satisfying the Stokes equations to leading order is given by

$$u_z = 0, \quad u_\sigma = \frac{1}{\sigma}\frac{\partial \psi}{\partial \phi}, \quad u_\phi = -\frac{\partial \psi}{\partial \sigma}, \tag{B 2}$$

where

$$\psi = E(z)\,\Psi(\sigma,\phi), \tag{B 3}$$

$$\sigma \ll 1, \tag{B 4}$$

$E(z)$ is an arbitary function, and Ψ is a stream function given by Moffat (1964) and Weinbaum (1968). For the case of interest here, $\phi_0 = \frac{3}{4}\pi$ and,

$$\Psi = \beta\sigma^\lambda\left[\cos\lambda\phi - \frac{\cos\lambda\phi_0}{\cos(\lambda-2)\phi_0}\cos(\lambda-2)\phi\right] + \gamma\sigma^\mu\left[\sin\mu\phi - \frac{\sin\mu\phi_0}{\sin(\mu-2)\phi_0}\sin(\mu-2)\phi\right] + \ldots, \tag{B 5}$$

where $\lambda = 1.544$, $\mu = 1.909$ and β and γ are constants. The eigenvalues λ and μ correspond to flow components which are antisymmetric and symmetric about $\phi = 0$, respectively. The given components are of particular interest since they give infinite shear (vorticity) on the walls as $\sigma \to 0$ (the vorticity from all other components tends to zero as $\sigma \to 0$).

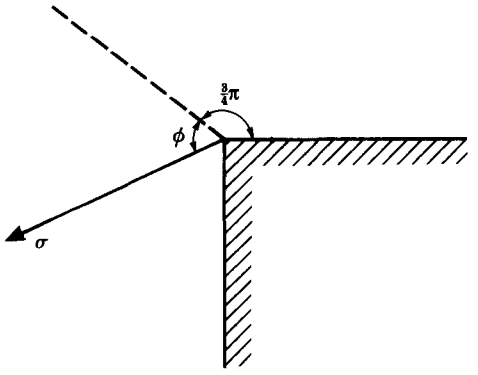

FIGURE 16. Coordinate system near a corner (z is normal to the page).

For a three-dimensional flow, the continuity equation is

$$\frac{\partial u_z}{\partial z}+\frac{1}{\sigma}\frac{\partial}{\partial\sigma}(\sigma u_\sigma)+\frac{1}{\sigma}\frac{\partial u_\phi}{\partial\phi}=0, \tag{B 6}$$

which suggests velocity components of the form:

$$u_z=\sigma^\nu U_z(z,\phi), \quad u_\sigma=\sigma^{\nu+1}U_\sigma(z,\phi), \quad u_\phi=\sigma^{\nu+1}U_\phi(z,\phi). \tag{B 7}$$

The vorticity vector can be calculated from (B 7) and substituted in the vorticity transport equation – the vector Laplacian of vorticity is zero. To leading order, the σ- and ϕ-equations are satisfied by

$$u_z=A(z)\,\sigma^{\nu_1}\cos\nu_1\phi+B(z)\,\sigma^{\nu_2}\sin\nu_2\phi, \tag{B 8}$$

where ν_1 and ν_2 correspond to symmetric and antisymmetric flows respectively, and A and B are arbitrary functions. Applying the boundary condition (B 1) gives

$$\nu_1=\frac{\frac{1}{2}\pi+m\pi}{\phi_0}, \quad \nu_2=\frac{\pi+m\pi}{\phi_0}; \quad m=0,1,2,\ldots. \tag{B 9}$$

Taking the symmetric component first the z-vorticity equation yields:

$$(\nu_1+2)\,U_\phi-\frac{\partial U_\sigma}{\partial\phi}=C(z)\cos\nu_1\phi+D(z)\sin\nu_1\phi, \tag{B 10}$$

where C and D are arbitrary, while the continuity equation (B 6) reduces to

$$A'(z)\cos\nu_1\phi+(\nu_1+2)\,U_\sigma+\frac{\partial U_\phi}{\partial\phi}=0. \tag{B 11}$$

Equations (B 10), (B 11) and the boundary conditions (B 1) now produce:

$$\left.\begin{aligned} u_z&=A(z)\,\sigma^{\nu_1}\cos\nu_1\phi,\\ u_\sigma&=-\frac{1}{\nu_1+2}A'(z)\,\sigma^{\nu_1+1}\cos\nu_1\phi,\\ u_\phi&=0. \end{aligned}\right\} \tag{B 12}$$

In a similar manner, the antisymmetric components are

$$\left.\begin{aligned} u_z &= B(z)\,\sigma^{\nu_2}\sin\nu_2\phi, \\ u_\sigma &= -\frac{1}{\nu_2+2}B'(z)\,\sigma^{\nu_2+1}\sin\nu_2\phi, \\ u_\phi &= 0. \end{aligned}\right\} \tag{B 13}$$

Equations (B 9), (B 12) and (B 13) give two sets of independent leading-order solutions which are valid for all ϕ_0. There is another independent solution, which has as its leading term

$$\left.\begin{aligned} u_z &= a(z)\,\sigma^2(\cos 2\phi-\cos 2\phi_0), \\ u_\sigma &= -\tfrac{1}{4}a'(z)\,\sigma^3(\cos 2\phi-\cos 2\phi_0), \\ u_\phi &= 0, \end{aligned}\right\} \tag{B 14}$$

if $\phi_0 \neq \frac{1}{4}\pi$ or $\frac{3}{4}\pi$, and

$$\left.\begin{aligned} u_z &= a(z)\,\sigma^2[\phi_0\sin 2\phi_0-\phi\sin 2\phi+(\ln\sigma)\cos 2\phi], \\ u_\sigma &= -\tfrac{1}{4}a'(z)\,\sigma^3[\phi_0\sin 2\phi_0-\phi\sin 2\phi-\tfrac{1}{4}\cos 2\phi+(\ln\sigma)\cos 2\phi], \\ u_\phi &= 0, \end{aligned}\right\} \tag{B 15}$$

if $\phi_0 = \frac{1}{4}\pi$ or $\frac{3}{4}\pi$. In fact, (B 14) reduces to (B 12) with $m = 0$ or 1 in (B 9) if $\phi_0 = \frac{1}{4}\pi$ or $\frac{3}{4}\pi$, respectively. The symmetric solutions obtained from dropping the z-dependence in (B 12)–(B 15) were found by Moffatt & Duffy (1980) who considered Poiseuille flow in an irregular shaped straight duct with a sharp corner.

The flows given by (B 12) and (B 13) have a relatively small $\partial p/\partial z$ – at most $O(\sigma^{\nu_1})$ – where p is the dimensionless pressure, while the flow given by (B 14) or (B 15) has $\partial p/\partial z = Ka(z)+O(\sigma^2)$, where K is a constant depending on ϕ_0. The latter will usually be the dominant part of $\partial p/\partial z$ as $\sigma\to 0$. Hence, $\partial p/\partial z$ is Poiseuille-like in that it does not depend on σ or ϕ to leading order (this does not, of course, imply that p is independent of σ and ϕ at leading order). Note also that as $\sigma\to 0$, u_z is the dominant part of the flow.

In the above, the functions $A(z)$, $(B(z)$, etc. are determined by matching to the outer flow, and unless they are constants, the solutions are not exact solutions of the Stokes equations but are the leading terms of series solutions. The four solutions obtained are independent, and each represents a two-dimensional flow; one, (B 2)–(B 5), a flow in a plane normal to the walls, and the others (B 12), (B 13), and (B 14) or (B 15), flows essentially along the edge $\sigma = 0$. It is stressed that, given the similarity form (B 7), the two-dimensional nature of these flows was derived, not assumed. As mentioned above, our solutions are generalizations of those of Moffatt (1964), Weinbaum (1966), and Moffatt & Duffy (1980). Because of the wasy they were obtained – taking all such similarity solutions of the vorticity transport equation, using these to derive the velocity components, then applying the boundary conditions – it appears that they are complete to the order given.

In general, not only are the four sets of solutions independent (although they may be linked by the outer flow), they have different orders with respect to σ, at least at leading order. There are two exceptions to this; when $\sigma_0 = \frac{1}{2}\pi$ (i.e. flow on a flat plate) the eigenvalues for the symmetric flow along the wall (B 12) and the antisymmetric component of the flow in a plane normal to the wall (B 2)–(B 5) coincide at leading order, with $\nu_1 = \lambda-1 = 1$, as do the eigenvalues for the antisymmetric flow (B 13)

and the symmetric component of (B 5), where $\nu_2 = \mu - 1 = 2$; and when $\phi_0 = \pi$ (i.e. flow at the edge of a flat plate) the symmetric flow (B 12) and both components of (B 5) are of the same order, with $\nu_1 = \lambda - 1 = \mu - 1 = \frac{1}{2}$. Hence, with $\phi_0 = \frac{1}{2}\pi$ or π there exists the possibility of a true three-dimensional flow when $\sigma \ll 1$.

So far we have not specified the order of importance of the various solutions given above. This depends on ϕ_0, and Moffatt & Duffy (1980) give a table listing the leading terms for the symmetric flow formed by (B 12) and (B 14) or (B 15). For the case of special interest here with $\phi_0 = \frac{3}{4}\pi$, we find that

$$\lambda - 1 < \mu - 1 < \nu_1 (m = 0) < \nu_2 (m = 0) < 2 = \nu_1 (m = 1).$$

Note that since $\nu_1 (m = 0) = \frac{2}{3} < 1$ and $\nu_2 (m = 0) = \frac{4}{3} > 1$, the terms corresponding to λ, μ, and $\nu_1 (m = 0)$ are the only terms that can give infinite vorticity as $\sigma \to 0$.

REFERENCES

Bramley, J. S. & Dennis, S. C. R. 1984 The numerical solution of a two-dimensional flow in a branching channel. *Computers & Fluids* **12**, 339–355.

Caro, C. E., Fitz-Gerald, J. M. & Schroter R. C. 1971 Atheroma and arterial wall shear. *Proc. R. Soc. Lond.* B **177**, 109–159.

Caro, C. G., Pedley, T. J., Schroter, R. C. & Seed, W. A. 1978 *The Mechanics of the Circulation.* Oxford University Press.

Chobanian, A. V. 1983 The influence of hypertension and other hemodynamic factors in atherogenesis. *Prog. Cardivascular Diseases* **26**, 177–196.

Cornhill, J. F. & Roach, M. R. 1976 A quantitative study of the localizaiton of atherosclerotic lesions in the rabbit aorta. *Atherosclerosis* **23**, 489–501.

Dagan, Z., Weinbaum, S. & Pfeffer, R. 1982 An infinite-series solution for the creeping motion through an orifice of infinite length. *J. Fluid Mech.* **115**, 505–523.

de Mestre, N. J. & Guiney, D. C. 1971 Low Reynolds number oscillatory flow through a hole in a wall. *J. Fluid Mech.* **47**, 657–666.

Dennis, S. C. R., Ingham, D. B. & Cook, R. N. 1979 Finite-difference methods for calculating steady incompressible flows in three-dimensions. *J. Comp. Phys.* **33**, 325–339.

Fry, D. L. 1973 Responses of the arterial wall to certain physical factors. *Ciba Found. Symp. 12, Atherogenesis: initiating factors*, pp. 93–120.

Higdon, J. J. L. 1985 Stokes flow in abitrary two-dimensional domains: shear flow over ridges and cavities. *J. Fluid Mech.* **159**, 195–226.

Lew, H. S. & Fung, Y. C. 1969 On the low Reynolds number entry flow into a circular cylindrical tube. *J. Biomech.* **2**, 105–119.

McDonald, D. A. 1974 *Blood Flow in Arteries.* Arnold.

Moffatt, H. K. 1964 Viscous and restive eddies near a sharp corner. *J. Fluid Mech.* **18**, 1–18.

Moffatt, H. K. & Duffy, B. R. 1980 Local similarity solutions and their limitations. *J. Fluid Mech.* **96**, 299–313.

Nerem, R. M. & Levesque, M. J. 1983 The case for fluid dynamics as a localizing factor in atherogenesis. In Schettler *et al.* (1983)

Nerem, R. M., Levesque, M. J. & Cornhill, J. F. 1981 Vascular endothelial morphology as an indicator of the pattern of blood flow. *J. Biomech. Engng* **103**, 172–176.

Parmet, I. L. & Saibel, E. 1965 Axisymmetric creeping flow from an orifice in a plane wall. *Commun. Pure Appl. Maths* **18**, 17–23.

Pedley, T. J. 1980 *The Fluid Mechanics of the Large Blood Vessels.* Cambridge University Press.

Sampson, R. A. 1891 On Stokes's current functions. *Phil. Trans. R. Soc. Lond.* A **182**, 449–518.

Schettler, G., Nerem, R. M., Schmidt-Schöbein, H., Mörle, H. & Diehm, C. (Eds) 1983 *Fluid Dynamics as a Localizing Factor for Atherosclerosis.* Springer.

SCHWARZ, C. J., SPRAGUE, E. A., FOWLER, S. R. & KELLEY, J. L. 1983 Cellular participation in atherogenesis: Selected facets of endothelium, smooth muscle, and the peripheral blood monocyte. In Schettler *et al.* (1983).

SCHWARZ, S. M., REIDY, M. A. & HANSSON, G. K. 1983 Injury at the vascular surface. In Schettler *et al.* (1983).

SHEN, C. & FLORYAN J. M. 1985 Low Reynolds number flow over cavities. *Phys. Fluids* **28**, 3191–3203.

SINZINGER, H., SILBERBAUER, K. & AUERSWALD, W. 1980 Quantitative investigation of sudanophilic lesions around the aortic ostia of human fetuses, newborn, and children. *Blood Vessels* **17**, 44–52.

SMITH, F. T. 1976 Pipeflows distorted by non-symmetric indentation or branching. *Mathematika* **23**, 62–83.

SOBEY, I. J. 1976 Bio-fluid dynamics of bifucations. Ph.D. thesis, University of Cambridge.

SOBEY, I. J. 1977 Laminar boundary-layer flow past a two-dimensional slot. *J. Fluid Mech.* **83**, 33–47.

STEINBERG, D. 1983 Lipoproteins and atherosclerosis. *Arteriosclerosis* **3**, 283–301.

TAKEMATSU, M. 1966 Slow viscous flow past a cavity. *J. Phys. Soc. Japan* **21**, 1816–1821.

TANEDA, S. 1979 Visualization of separating Stokes flows. *J. Phys. Soc. Japan* **46**, 1935–1942.

WEINBAUM, S. 1968 On the singular points in the laminar two-dimensional near wake flow field. *J. Fluid Mech.* **33**, 38–63.

WEINBAUM, S., TZEGHAI, G., GANATOS, P., PFEFFER, R. & CHIEN, S. 1985 Effect of cell turnover and leaky junctions on arterial macromolecular transport. *Am. J. Physiol.* **248**, H945–H960.

WOODS, L. C. 1954 A note on the numerical solution of fourth-order differential equations. *Aero. Q.* **5**, 176.